

AD-A245 184



2

**FINAL TECHNICAL REPORT
PHASE II SBIR
CONTRACT NO. N00019-87-C-0267**

**MONOLITHIC INTEGRATION OF A DFB SUPERLATTICE
LASER USING HIGH ENERGY ION IMPLANTATION**

PREPARED BY

P.P. Pronko, A.K. Rai, D. Ingram, A.W. McCormick and A. Ezis

PREPARED FOR

Naval Air Systems Command

SUBMITTED BY

UES, Inc.
4401 Dayton-Xenia Road
Dayton, OH 45432
(513) 426-6900

**DTIC
ELECTE
JAN 30 1992
S B D**



92 1 28 062

92-02281



REPORT DOCUMENTATION PAGE

Form Approved
OMB No. 0704-0188

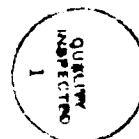
1. REPORT SECURITY CLASSIFICATION N/A		1b. RESTRICTIVE MARKINGS N/A	
2. SECURITY CLASSIFICATION AUTHORITY N/A		3. DISTRIBUTION/AVAILABILITY OF REPORT Approved for Public Release; Distribution is Unlimited.	
4. DECLASSIFICATION/DOWNGRADING SCHEDULE N/A		5. MONITORING ORGANIZATION REPORT NUMBER(S)	
PERFORMING ORGANIZATION REPORT NUMBER(S) UES Project 889		6. OFFICE SYMBOL (If applicable) N/A	
1. NAME OF PERFORMING ORGANIZATION UES, Inc.		7a. NAME OF MONITORING ORGANIZATION Department of the Navy	
2. ADDRESS (City, State, and ZIP Code) 401 Dayton-Xenia Road Dayton, OH 45432		7b. ADDRESS (City, State, and ZIP Code) Naval Air Systems Command Washington, DC 20361-5360	
8a. NAME OF FUNDING/SPONSORING ORGANIZATION Department of the Navy		8b. OFFICE SYMBOL (If applicable) AIR-536T	
9. PROCUREMENT INSTRUMENT IDENTIFICATION NUMBER N00019-87-C-0267		10. SOURCE OF FUNDING NUMBERS	
11. ADDRESS (City, State, and ZIP Code) Naval Air Systems Command Washington, DC 20361-5360		PROGRAM ELEMENT NO. 65502N	PROJECT NO.
		TASK NO.	WORK UNIT ACCESSION NO.
1. TITLE (Include Security Classification) MONOLITHIC INTEGRATION OF A DFB SUPERLATTICE LASER USING HIGH ENERGY ION IMPLANTATION			
2. PERSONAL AUTHOR(S) P. Pronko, A. K. Rai, D. Ingram, A. W. McCormick and A. Ezis			
3a. TYPE OF REPORT Final	13b. TIME COVERED FROM 09/30/87 to 03/29/90	14. DATE OF REPORT (Year, Month, Day) 02/13/91	15. PAGE COUNT 84
6. SUPPLEMENTARY NOTATION			
7. COSATI CODES		18. SUBJECT TERMS (Continue on reverse if necessary and identify by block number)	
FIELD	GROUP	SUB-GROUP	
09	03		
20	12		
9. ABSTRACT The objective of this research is to develop the use of high energy (MeV) and medium energy (keV) ion beams for the purpose of selectively modifying the optical properties of superlattice systems consisting of mixed III-V compound semiconductors. In particular, the research was directed at the AlGaAs/GaAs multilayer superlattice system and its potential use in fabricating a monolithically integrated distributed feedback laser for use in optoelectronic circuits. The optical properties of such semiconductor superlattice systems have been shown to be sensitive to ion bombardment and its associated implantation and mixing process. The use of ion beams makes it possible to modify these structures through selective masking so that optical elements such as lasers, waveguides, and switches could be fabricated under the constraints imposed by monolithic integration. In particular, investigations were made into the effects of implantation controlled disordering of AlGaAs and GaAs through impurity, defect, and ion beam mixing effects. The results of this work were applied to the development and fabrication of an ion implanted distributed feedback (DFB) type laser in a multilayer superlattice system.			
20. DISTRIBUTION/AVAILABILITY OF ABSTRACT <input type="checkbox"/> UNCLASSIFIED/UNLIMITED <input checked="" type="checkbox"/> SAME AS RPT <input type="checkbox"/> DTIC USERS		21. ABSTRACT SECURITY CLASSIFICATION N/A	
22a. NAME OF RESPONSIBLE INDIVIDUAL Dr. Slotter, Department of the Navy		22b. TELEPHONE (include Area Code) (703)692-2616	22c. OFFICE SYMBOL AIR-536T

TABLE OF CONTENTS

SECTION	PAGE
LIST OF ILLUSTRATIONS	iv
1.0 INTRODUCTION	1
1.1 Background	1
1.2 Monolithically Integrated Lasers and the DFB Concept	4
1.2.1 Distributed Feedback Laser Properties	5
1.3 Program Approach and Review of Statement of Work	8
1.3.1 Results from Phase I Research	9
1.3.2 Approach to the Phase II Program	11
1.3.2.1 Optical Characterization	11
1.3.3 Phase II Research Program	12
1.3.3.1 Ion Implantation Disordering Study	12
1.3.3.2 Grating Fabrication and Testing	13
2.0 FABRICATION OF ALTERNATING REFRACTIVE INDEX GRATING	14
2.1 Refractive Index of Quantum Well Superlattices versus Compositionally Alloyed AlGaAs	14
2.1.1 Refractive Index of Bulk Alloyed AlGaAs	14
2.1.2 Refractive Index of Quantum Well-Superlattice Composed of GaAs/AlAs or GaAs/AlGaAs	16
2.2 Ion Mixing for Chemical Disordering	16
3.0 OPTICAL PROPERTIES OF MULTIPLE QUANTUM WELL ARRAYS AND THEIR RELATION TO DFB LASER DESIGN ...	18
3.1 Introduction	18
3.1.1 Multi-Quantum Well/Superlattice Material Fabricated by Molecular Beam Epitaxial Crystal Growth	21
3.2 Spontaneous Photoluminescence of the MBE Material	23
3.3 Coupling of Energy Levels Between the SL and QW	27
3.4 Photopumped Laser Operation	32
3.5 Annealing of the Multiple Quantum Well Array	40
3.6 Summary and Conclusions of Optical Properties for QW/SL Arrays	43
3.7 Considerations Relative to DFB/DBR Laser Fabrication	46
4.0 Materials Evaluation of Multi-Quantum Well/Superlattice Samples Fabricated by Molecular Beam Epitaxy	47
4.1 Cross-Sectional Transmission Electron Microscopy (X-TEM) for Structural Analysis	47
4.2 Sputter Auger Compositional Profiling	48

TABLE OF CONTENTS (CONT'D.)

SECTION		PAGE
5.0	ION MIXING IN SUPERLATTICE SYSTEMS	51
5.1	Superlattice Disordering from Cascade Mixing Under Ga Ion Implantation	54
5.1.1	Ga Implantation in GaAs - Calibration of Cascade Damage Production	56
5.1.2	Ga Implantation in AlGaAs/GaAs S/L and Bulk AlGaAs	57
5.1.3	Annealing of Ga Implanted S/L Material	62
5.2	Superlattice Disordering Under Si Ion Implantation	66
REFERENCES	72
APPENDIX I	I-1



Accession For	
NTIS GRA&I	<input checked="" type="checkbox"/>
DTIC TAB	<input type="checkbox"/>
Unannounced	<input type="checkbox"/>
Justification	
By _____	
Distribution/	
Availability Codes	
Dist	Avail and/or Special
A-1	*

LIST OF ILLUSTRATIONS

FIGURE		PAGE
1	Schematic Illustration of DFB and DBR Lasers. (After Agrawal and Dutta [1])	6
2	Illustration of Mode Spectrum and the Required Threshold Gains for Index Periodicity	7
3	Index of Refraction n of $\text{Ga}_{1-x}\text{Al}_x\text{As}$ as a Function of Al Concentration	15
4	Index of Refraction $n(\omega)$ for GaAs-AlAs Superlattices as a Function of their Structure	17
5	Comparison of Experimental (Dashed Line) and Theoretical (Solid Line) Data on Refractive Index as a Function of Energy (eV)	17
6	Schematic Diagram of the GaAs/AlGaAs Superlattice and Quantum Well Laser Structure	20
7	Schematic Diagram of the Implanted Superlattice Forming a Grating for Distributed Feedback	20
8	Spontaneous Emission from Three Different Quantum Well/ Superlattice Samples with Different Layer Thicknesses	24
9	Spontaneous Emission from the Samples of Figure 8 at Higher Pumping Power	25
10	Energy Band Diagram for the Multiple Quantum Well Array. Large QW = 260Å; SL with 30Å Wells and Barriers	28
11	Selected Wave Functions for the Potential of Figure 10	29
12	Energy Band Diagram for Multiple Quantum Well Array. Large QW = 350Å; SL with 55Å Wells and Barriers	31
13	Selected Wavefunctions for the Potential of Figure 12	33
14	Stimulated Emission for a Typical Platelet ($24\text{ }\mu\text{m} \times 258\text{ }\mu\text{m}$) with 60Å SL Layers and a 350Å QW	35
15	Stimulated Emission for a Platelet ($44\text{ }\mu\text{m} \times 255\text{ }\mu\text{m}$) with 30Å SL Layers and a 260Å QW	37

LIST OF ILLUSTRATIONS (CONT'D.)

FIGURE		PAGE
16	Stimulated Emission for a Platelet ($41\ \mu\text{m} \times 415\ \mu\text{m}$) with Same Structure as Figure 15	38
17	Stimulated Emission for a Platelet ($32\ \mu\text{m} \times 133\ \mu\text{m}$) with SL Region only and no QW	39
18	Comparison of Spontaneous Emission from As-Grown Sample and Samples Annealed in Ga or As Over Pressure	41
19	Platelet Spectra ($25\ \mu\text{m} \times 138\ \mu\text{m}$) from Sample Annealed in As Over Pressure	42
20	Emission from Platelet ($30\ \mu\text{m} \times 240\ \mu\text{m}$) Made from Sample Annealed in As Over Pressure	44
21	X-TEM Bright Field Micrograph of a Multi-Quantum Well/ Superlattice (MQW/SL) Used in These Experiments	48
22	Schematic of TEM Sample Preparation	49
23	Low Resolution Auger Compositional Depth Profile of Entire Thickness of QW/SL Sample	50
24	High Resolution Auger Compositional Depth Profile of First Half of QW/SL Sample	51
25	Initial Design and Structure of MQW/SL - DFB Laser	52
26	Block Diagram Showing Approaches to Fabricating Ion Mixed Grating Structure for DFB Laser Application	53
27	RBS-Channeling Spectra. 960 keV Ga Implanted GaAs	56
28	RBS-Channeling Spectra. 960 keV Ga Implanted MQW/SL of Figure 21	58
29	X-TEM MQW/SL of Figure 21 After Implant. $960\ \text{keV}$, $1 \times 10^{14}\ \text{cm}^{-2}\ \text{Ga}$	58
30	RBS Channeling Spectra. 890 keV Ga Implanted AlGaAs	59
31	RBS-Channeling Spectra. 890 keV Ga Implanted MQW/SL of Figure 21	60

LIST OF ILLUSTRATIONS (CONT'D.)

FIGURE		PAGE
32	Auger Al Composition Depth Profiles of Ga ⁺ Implanted QW/SL Samples	61
33	Dark Field TEM Cross Section Micrographs of QW/SL Material After Implantation with (a) 5×10 ¹⁴ and (b) 1×10 ¹⁶ cm ⁻² Fluences of 890 keV Ga ⁺ Ions	63
34	Dark Field TEM Cross Section Micrographs of QW/SL Material After Implantation with (a) 1×10 ¹⁵ and (b) 1×10 ¹⁶ cm ⁻² Fluences of 890 keV Ga ⁺ Ions and Annealing at 850°C for 1 min	64
35	Bright Field TEM Cross Section Micrographs of QW/SL Material After Implantation with (a) 1×10 ¹⁴ , (b) 1×10 ¹⁵ , and (c) 1×10 ¹⁶ cm ⁻² Fluences of 890 keV Ga ⁺ Ions and Annealing at 850°C for 1 min	65
36	SIMS Impurity Profile of Broad Beam Implanted Quantum Well Laser Material (Dose = 1×10 ¹⁵ cm ⁻²)	67
37	SIMS Impurity Profile of Broad Beam Implanted Quantum Well Laser Material (Dose = 5×10 ¹⁵ cm ⁻²)	68
38	SIMS Impurity Profile of Broad Beam Implanted Quantum Well Laser Material (Dose = 1×10 ¹⁶ cm ⁻²)	69
39	TEM Cross Sections of Laser Material Implanted with (a) 5×10 ¹³ cm ⁻² , (b) 5×10 ¹⁴ cm ⁻² Doses of 250 keV Si ⁺ Ions and Annealed at 1050°C for 10 seconds	70
40	TEM Cross Sections of Laser Material Implanted with (a) 1×10 ¹⁵ cm ⁻² , (b) 1×10 ¹⁶ cm ⁻² Doses of 250 keV Si ⁺ Ions and Annealed at 1050°C for 10 seconds	71
41	Ion Range and Damage Profiles for Al _{0.3} Ga _{0.7} As Implanted with 890 keV Ga	I-2
42	Ion Range and Damage Profiles for Al _{0.3} Ga _{0.7} As Implanted with 960 keV Ga	I-3
43	Ion Range and Damage Profiles for Al _{0.3} Ga _{0.7} As Implanted with 250 keV Si	I-4

1.0 INTRODUCTION

The objective of this research is to develop the use of high energy (MeV) and medium energy (keV) ion beams for the purpose of selectively modifying the optical properties of superlattice systems consisting of mixed III-V compound semiconductors. In particular, the research was directed at the AlGaAs/GaAs multilayer superlattice system and its potential use in fabricating a monolithically integrated distributed feedback laser for use in optoelectronic circuits. The optical properties of such semiconductor superlattice systems have been shown to be sensitive to ion bombardment and its associated implantation and mixing process. The use of ion beams makes it possible to modify these structures through selective masking so that optical elements such as lasers, waveguides, and switches could be fabricated under the constraints imposed by monolithic integration. In particular, investigations were made into the effects of implantation controlled disordering of AlGaAs and GaAs through impurity, defect, and ion beam mixing effects. The results of this work were applied to the development and fabrication of an ion implanted distributed feedback (DFB) type laser in a multilayer superlattice system.

It is anticipated that this work will result in information leading to controlled fabrication of miniature optical elements monolithically integrated into optoelectronic systems. In particular, it will contribute to an understanding of the use of high energy ion beams for fabricating such devices as laser elements and their use in two- and three-dimensional optical and digital signal processing systems.

1.1 BACKGROUND

Integrated optoelectronic circuits for telecommunications applications will eventually consist of single semiconductor chips with integrated transmitters made up of lasers and electronic support circuitry. This circuitry will drive the lasers as well as monitor, stabilize, and shape its light pulses. The receiver end of a chip will include amplifiers, equalizers, and pulse reshapers as well as photodetectors.

Our interest in the present study is in the development of technology for the fabrication of the integrated laser devices which will be embedded in the transmitter section of the III-V semiconductor chip. This technology is envisioned to involve the use of thin epitaxial films, high energy ion implantation, and patterned lithography. The achievement of such integrated optoelectronic circuits would provide greater reliability, circuit density, and speed compared to that available in hybrid systems. The value of total integration on a single material substrate such as alloyed GaAs is that production requirements of electronic and optical devices can be met by a single material and a single basic production process rather than two or more materials and variety of production processes.

An important advantage of integration is the reduction of interconnection problems that occur during signal conversions between optical and electronic states. For example, a single integrated optoelectronic circuit might link electronic circuits with optical fibers. In so doing it could replace an otherwise elaborate interface with a very much simpler set of components. Since integration reduces unwanted path delays and other complications associated with electrical interconnections, the integrated device would be faster and less noisy. Inherent in this would also be greater stability. Ultimately, this could lead to the handling of coherent optical waves in small, densely packed configurations.

Special problems will be encountered in developing reliable monolithic systems. Production yields will be critically important and these will depend very much on the quality and uniformity of the substrate material. These yields will have to be improved if wafer scale integration is to become commercially acceptable. Yields of 50 to 70 percent are possible, however, improvements over and above this level will be necessary. Since the devices in the integrated system are made of multilayer structures, their production on a routine basis will be difficult. Significantly, the total yield of a monolithic integrated semiconductor system is the yield of the laser light source, multiplied by the yield of the electronics, multiplied by the yield of the waveguide circuit, multiplied by the yield of the detector array. It becomes obvious that each device that is a part of this system will have to be fabricated in the simplest most direct minimum step process possible. A serious consideration in developing these systems is the general compatibility of devices in the systems. An important example of this is the fact that

monolithic integration of a semiconductor laser and an electro-optical guided wave circuit requires that the laser cavity be formed by a distributed feedback or distributed Bragg reflection laser in order that the output beam be directly in the waveguide plane. The fabrication of such lasers is now a complex process involving a grating etching procedure which is intricate and much less attractive than the high energy ion beam approach being proposed in this work.

The recent emergence of single mode optical fiber waveguides has been an important factor in the continued and expanded interest in integrated-optic devices that operate in the single mode state. Fiber waveguides of 50 to 100 μm diameter can normally support hundreds of E-M modes simultaneously and are, therefore, referred to as multimode fibers. However, when the diameter of a waveguide is brought down to 4 or 5 μm , it can support only a single optical mode at a specified wavelength. These single mode fibers do not display the interference effects from multiple E X B fields that cause dispersion in thicker multimode fibers. Dramatic reductions in propagation losses are realized in single mode fibers. However, in order to take advantage of this effect, stable single frequency light sources are required. The distributed feedback (DFB) laser or alternatively a distributed Bragg reflection (DBR) laser is ideally suited for this purpose. In addition to its being a single mode single wavelength device, it is also an in-line device with a small emittance solid angle which is conducive to minimization of fiber coupled insertion losses. It is also probable that newly developed coupler switch modulators will be used with these light sources to allow them to run continuously in a stable temperature range, thereby eliminating transient "chirping" effects associated with direct current modulation that can cause temperature and, therefore, wavelength shifts. Such external integrated optic modulators are currently under development. Configurations of this type are expected to effectively eliminate modal noise in these optical processing systems. Continuous DC operation of the laser will also result in longer laser operating lifetime compared to the on-off switching mode. Ultimately, DFB or DBR lasers could be bundled together, each using a different wavelength, having their outputs multiplexed into a single mode fiber, thereby transmitting multiple optical signals simultaneously on a single line for long distance communications.

1.2 MONOLITHICALLY INTEGRATED LASERS AND THE DFB CONCEPT

Elementary laser diodes can be monolithically integrated into an optical circuit, however, they depend on optical feedback from a pair of reflecting surfaces in order to operate. These surfaces are needed to form the standard Fabry-Perot laser cavity. In an optical integrated circuit where the laser diodes are monolithically integrated within the semiconductor wafer, it is usually very difficult to form such reflecting surfaces. Etching or cleaving can be used, however, this will disrupt the planar surface of the wafer leading to difficulties in other aspects of circuit assembly. The use of an integrated distributed feedbacks grating, however, provides the necessary optical feedback while preserving normal planar surface geometry.

Operationally a DFB or DBR process relies on the use of a grating structure to create a periodic change in the index of refraction. This grating periodicity provides 180-degree reflections at specific wavelengths which depend on grating spacing. Present technology uses an etching process to corrugate the interface between two of the semiconductor layers that comprise the laser. This is done in a way where alternating segments of the corrugation have repetitively changing index of refraction. The production of these alternating refractive index segments using energetic ion beams is one of the primary objective of the present work. It is our intention to use ion implantation as a compositional disordering agent.

The Bragg condition for coherent wavefront reflection from a grating is $2d \sin \theta = \ell \lambda$ where d is the grating spacing, θ the reflection angle, λ the wavelength of the light and ℓ an integer. In a corrugated DFB grating where reflection is 180 degrees onto the incoming pitch of the wave the Bragg angle is $\theta = 90$ degrees and the coherence reflection equation reduces to $2d = \ell(\lambda_0/N_g)$ where N_g is the effective index of refraction in the waveguide for the mode under consideration. The vacuum wavelength of light that will be reflected through 180 degrees will then be $\lambda_0 = 2dN_g/\ell$. Although the laser can reflect many different longitudinal modes for the various values of ℓ , usually only one mode will lie within the gain bandwidth of the laser. Normally, gratings corresponding to $\ell = 3$ are most easily fabricated and result in a compromised minimum transverse scattering loss from the grating. Minimum losses occur for $\ell = 1$; however, this requires minimum grating spacing and cannot always be achieved under the fabrication

condition being used. Design considerations for a DFB grating and laser are given below in this section and in later sections.

1.2.1 Distributed Feedback Laser Properties

In a Fabry-Perot cavity, the feedback is provided by facet reflections where the magnitude of the reflectivity is essentially the same for all the longitudinal modes. The longitudinal mode discrimination is provided by the gain spectrum itself which is typically much wider than the longitudinal mode spacing. This results in poor mode discrimination since the mode closest to the gain peak is the most intense, but much of the output power is carried by other longitudinal modes. With rapid modulation, the power content increases in the side modes [1]. For many applications such as optical information processing, local area networks, and optical measurements, it is desirable to obtain laser diode emission predominantly in a single longitudinal mode even under high speed modulation.

In the DFB configuration, the feedback is frequency dependent with the cavity losses differing for different modes. Schematic diagrams of DFB and DBR lasers are shown in Figure 1. The periodic change in the index of refraction is achieved by the corrugation in the gain medium. Materials of differing indices of refraction are on opposite sides of the grating. The feedback mechanism allows for mode stability and spectral purity.

The grating is generally placed in the cladding layers in order to decrease the possibility of introducing defects in the active region and to avoid increasing the rate of nonradiative recombination. As a result, the coupling is through the evanescent wave in the structure. High quality GaAs/AlGaAs devices have been demonstrated that operate continuously at room temperature with low threshold currents, good mode stability, and good current confinement [2-5].

The grating, which needs to be of submicron dimensions in order to be effective, is generally made by a photolithographic process such as holographic or electron-beam lithography and subsequent etching such as reactive-ion etching, wet chemical etching, or ion-milling.

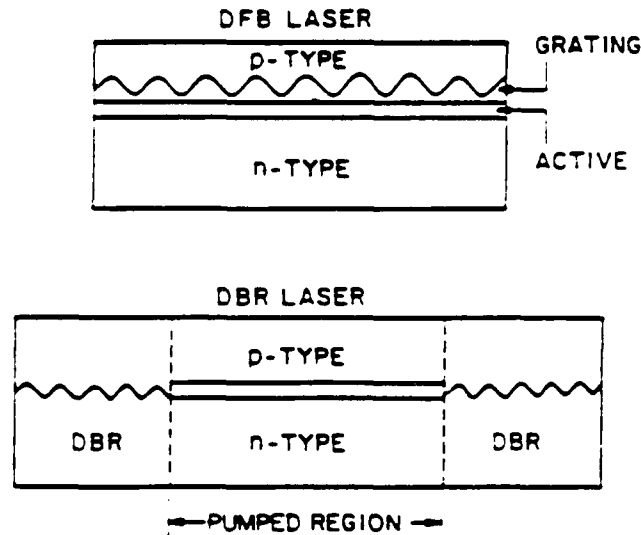


Figure 1. Schematic Illustration of DFB and DBR Lasers. (After Agrawal and Dutta [1])

Problems arise however, in the regrowing of epitaxial layers on top of the diffraction grating and in producing low order gratings. For example, a first order grating with laser emission at 8700\AA (GaAs at room temperature) requires a grating period on the order of 1250\AA .

The temperature dependence of a DFB laser, $d\lambda/dT \approx 0.5\text{\AA}/\text{K}$, is much smaller than that of a Fabry-Perot laser, $d\lambda/dT \approx 3.7\text{\AA}/\text{K}$ [6], because of the wavelength dependence of the feedback. The temperature dependence of a DFB laser follows the temperature dependence of the coefficient of refractive index of GaAs, whereas the temperature dependence of a Fabry-Perot laser follows the temperature dependence of the gain peak.

Another advantage of DFB lasers is that surface emission is supported by even order gratings [7]. The output coupling is along the entire length of the device which results in a broad area, low power density, highly collimated laser [8-10]. Surface emission could prove to be an effective way to couple light out of a circuit, and it can also be used in the development of monolithic laser arrays.

According to the coupled wave theory of Kogelnik and Shank [11], there is no resonance at the Bragg wavelength for an axially symmetric periodic resonator with index coupling. The lasing spectrum has two lowest threshold modes, one on each side of the "stop band." The stop

band, in which propagation is forbidden, is centered at the Bragg wavelength and it is several \AA to a few tens of \AA wide [12]. Figure 2 shows the threshold variation of the modes supported in a DFB laser with non-reflecting mirrors. This two mode degeneracy can cause failures in high-data-rate communication systems, and it needs to be controlled in order to achieve consistent single mode operation.

In practice, many devices show single frequency operation, since the gain degeneracy can be broken by cleaved facets [13,14]. Single mode operation is not guaranteed, however, since the relative position of the reflector and the grating is of critical importance. Depending on the phase of the grating at the facet, either single or multi-mode operation can be supported by the laser [15].

To stabilize the device, a $\lambda/4$ phase shift can be introduced at the center of the grating, or an asymmetry can be created in the structure by means of a facet reflection to favor one mode [12]. The $\lambda/4$ phase shift enables the resonant mode to be at the center of the stop band where the feedback is the strongest and the required threshold gain is the lowest [11]. Additionally, current can be applied to two separate electrodes on an ordinary uniform grating. This adjustment can provide stable single frequency operation at either mode, or high speed switching between the two modes. The injected current to one section relative to the other varies the index of refraction and can result in a continuous tuning of the Bragg wavelength [12,16].

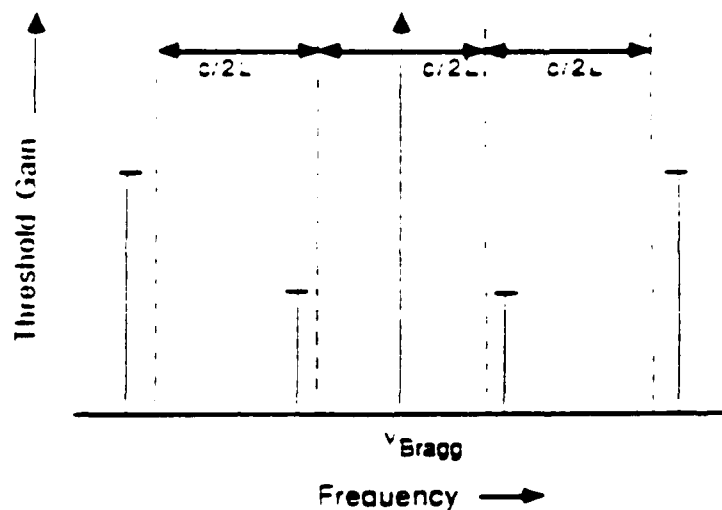


Figure 2. Illustration of Mode Spectrum and the Required Threshold Gains for Index Periodicity [11].

DBR lasers are basically Fabry-Perot lasers with end mirrors that exhibit frequency-dependent reflectivity. Lasing occurs at the wavelength for which the reflectivity is a maximum. There is no stop band since there is no distributed feedback within the DBR cavity, and the lowest threshold mode occurs close to the Bragg wavelength. The optical losses in the DBR regions can be high due to the absorption in the unpumped regions. The coupling losses can also be high, especially if the grating is located in the cladding layers, and generally lower order gratings are most effective. The spectral characteristics of DBR and DFB lasers are very similar.

1.3 PROGRAM APPROACH AND REVIEW OF STATEMENT OF WORK

The goal of the overall effort being developed here is the use of ion beam techniques for modifying the optical properties of III-V superlattice systems. Specific attention is being directed at the GaAs/AlGaAs system and its potential application to laser light sources for integrated optoelectronic systems. Other optical element devices such as switches, modulators, couplers, and filters could also benefit from this work.

In order to develop the specific laser system of interest, namely a DFB or DBR laser, it is necessary to achieve the ability to controllably modify the optical properties of the superlattice by ion implantation. This is necessary in order to fabricate the tunable distributed feedback grating that is central to these type lasers. Compositional disordering from the effects of the ion implantation is therefore the immediate first step to be accomplished. This disordering process must be highly controllable if it is to be expected to work. Control must be exercised over the depth of disordering, the final chemical composition of the disordered region, the amount of mask edge scattering, the amount of diffusional broadening that occurs under annealing, and the final defect state and crystal perfection of the disordered region. Accomplishing this and simultaneously producing the appropriate optical properties of the disordered region presents a substantial research effort in itself. This, however, is only the first step in fabricating an operational laser using this manufacturing method. Design and assembly of the laser device must also be accomplished.

Therefore, the three major work segments to the overall effort are:

- (1) Develop a superlattice disordering procedure using ion implantation or irradiation.
- (2) Develop a submicron grating for use as a distributed feedback device.
- (3) Design and develop a DFB or DBR solid state laser compatible for use in optoelectronic circuits.

The specific details of ion beam type, energy, and fluence for producing the disorder are related to the actual DFB grating design. Also, the design of the grating depends on the refractive index changes to be expected from the disordering process. We, therefore, see the superlattice disordering research and the device development proceeding hand in hand. The final objective is to produce an operating injection type DFB laser fabricated by ion implantation. This technology would eliminate the need for the cumbersome etching procedures now used in fabricating DFB gratings.

1.3.1 Results from Phase I Research

The sequence of experiments performed in Phase I were as follows:

- (1) Obtain and characterize starting AlGaAs/GaAs material.
- (2) Modify starting material using high energy ion beam mixing of AlGaAs in GaAs.
- (3) Evaluate and characterize the structural and chemical properties of the modified material.
- (4) Determine the extent to which optical properties are appropriately modified as a result of the materials changes produced in the high energy ion irradiation procedure.

- (5) Use these optical property changes in assessing their application to the design and development of optical waveguides and DFB laser devices.

The results of our Phase I work, as reported in the Phase I final report, showed that under heavy ion irradiation an originally sharp interface between AlGaAs and GaAs in a heterojunction will become graded through the redistribution of the Al across that interface by ion beam mixing. The optical properties of the heterostructure material before implantation compared to after implantation and annealing change by amounts in excess of 10 percent as a result of the redistribution of Al. This level of change argues in favor of waveguideing and distributed feedback. Interestingly, the production of amorphous material as a consequence of the ion bombardment results in very large changes in optical properties.

Implantation of Ga^+ ions along an Au mask edge was tested at a beam energy of 0.75 MeV. Damage effects under the mask due to edge scattering were found to be minimal. Clustered point defects were found to extend about 150\AA under the mask edge. This is considered an insignificant distance compared to the anticipated mask width of 2500\AA .

Specifically, Ga^+ ion implantation has been shown to affect the following properties of the AlGaAs/GaAs heterojunction that was investigated:

- (1) The Al/Ga ratio.
- (2) Thickness of the AlGaAs layer.
- (3) The complex dielectric constant $\tilde{\epsilon}$ (ϵ^1 , ϵ^2).
- (4) The reflectance R.

The changes induced in these optical properties are encouraging from the point of view of their being able to confine a laser beam in an optical waveguide or be used for the fabrication of a distributed feedback laser.

1.3.2 Approach to the Phase II Program

High energy (400 keV to 6 MeV) heavy and light ion implantation and irradiation have been performed with the UES Tandetron accelerator. This system has been used extensively on a contractual and service basis for ion implantation in GaAs based systems. Fluences from 10^{11} to 10^{16} ions/cm² are available on the machine. Beams of Si, Ga, and Al are readily available for the proposed study. A large number of other beams are also accessible.

Electron microscopy has been used for microstructure and irradiation damage analysis, crystal quality evaluation, and post anneal residual defect analysis. Plan view, cross-sectional view, and energy dispersive x-ray (EDX) analysis are available.

The MeV Ion Accelerator has been used to perform Rutherford backscattering spectrometry (RBS) and He⁺ ion channeling. These techniques are used to evaluate damage depth distributions, crystal quality, and impurity profiles. This work was performed at the UES Materials Lab.

Multilayer constituent and impurity profiling has been obtained by Auger electron spectroscopy (AES) under a subcontract with the University of Dayton's Surface Science Group.

1.3.2.1 Optical Characterization

This work was performed at North Carolina State University (NCSU).

- (1) Photoluminescence - Evaluate quality of disordered material (20K to 320K temperature range) before and after annealing.
- (2) High level optical excitation (Photo-Pumping) - Determine laser quality of fabricated materials without the need to develop a p-n junction system. This work is performed with a cavity dumped Argon ion laser (20K to 320K temperature range).

1.3.3 Phase II Research Program

The research program was undertaken in three segments:

- (1) Study and optimize ion implantation and irradiation as a procedure for changing the optical properties of quantum well heterostructure and superlattices in a controllable fashion.
- (2) Develop a submicron grating mask to be used as an implantation mask for high energy heavy ions and employ it in the fabrication of a photopumped test laser.
- (3) Test grating system using optical Photo Pumping as described above.

1.3.3.1 Ion Implantation Disorder Study

- (1) Using a selection of ions including, but not restricted to, Al, Ga, and Si, determine the most suitable ion and condition for creating long and short range compositional disorder in AlGaAs/GaAs superlattices and multilayers. Distinguish between contributions from defect induced disorder. Establish the extent to which a fast diffuser like Si will cause disorder broadening below a mask edge compared to slow diffusers such as Al and Ga.
- (2) Determine the level of crystal damage recovery in AlGaAs/GaAs under thermal annealing using both furnace and rapid thermal annealing (RTA). Establish the relationship between chemical disorder and the quality of recrystallization. Determine the nature of residual defects after annealing and investigate their potential impact on burn out of laser devices.
- (3) Investigate the effects of items 1 and 2 above as a function of implant fluence and anneal temperature to determine the optimum conditions for producing the desired

disorder. Implant fluences range from $5 \times 10^{13} \text{ cm}^{-2}$ to $5 \times 10^{15} \text{ cm}^{-2}$. Ion energies range from 400 keV to 3 MeV. Annealing temperatures range from 650 to 950°C.

- (4) Using ellipsometry and photoluminescence, measure the effects of the disordering (after annealing) on the optical properties of the AlGaAs/GaAs multilayer material. Use these results to design and test elementary waveguiding and DFB operation.

1.3.3.2 Grating Fabrication and Testing

This part of the program is devoted to the definition and development of a masking and implantation procedure to generate an optical grating structure consistent with the distributed feedback geometries required for a single mode, single wavelength solid state laser operating in the range of 0.7 to 1 μm . This essentially involves the fabrication of embedded multiple thin film selective partial reflection mirrors in a superlattice laser as part of an overall integrated optical circuit.

- (1) Develop a masking system or beam writing capability and implant geometry that would result in a grating pattern, after implantation, of approximately 0.25 μm spacing and approximately 0.5 to 1 μm in height.
- (2) Investigate lateral spreading of the ion beam below the mask (from multiple scattering or diffusion) as a fundamental limitation of the fine-line geometry achievable by this method.
- (3) Use the mask or beam writing capability developed in items 1 and 2 above to fabricate a DFB grating on an AlGaAs/GaAs laser structure and test the distributed feedback operation using photopumping.

2.0 FABRICATION OF ALTERNATING REFRACTIVE INDEX GRATING

The use of energetic ion beams for fabricating a DFB or DBR solid state laser grating represents a significant simplification over the etching and re-deposition procedures now used in making these gratings [17]. Ion implantation has been used for a broad range of electronic device fabrication steps in the past and we anticipate an important and useful role for it in the optoelectronics field as well.

2.1 REFRACTIVE INDEX OF QUANTUM WELL SUPERLATTICES VERSUS COMPOSITIONALLY ALLOYED AlGaAs

In order to properly understand the production of alternating refractive index gratings by ion implantation and ion mixing, it is instructive to first discuss the refractive index properties of quantum well superlattices versus that of bulk alloyed AlGaAs.

A superlattice system composed of GaAs/AlAs or GaAs/AlGaAs will have an average concentration of Al across a large number of periods which will depend on the relative thickness of each alternating layer and the aluminum concentration within the aluminum bearing component of the superlattice. Each material in the multi-layer stack will have its own independent refractive index; however, the optical properties of the system will depend on the structure and the average value of the Al concentration in the system. To a larger extent, however, it will be very much controlled by the quantum well nature of the periodic structure in the system of layers. The overall optical properties of the superlattice will be controlled primarily by the electronic energy states within the quantum wells. In bulk alloyed AlGaAs material the refractive index is controlled by the bulk Al concentration through the more usual velocity of light considerations in a solid.

2.1.1 Refractive Index of Bulk Alloyed AlGaAs

Figure 3 shows how the index of refraction n is expected to change as a function of Al content in bulk AlGaAs [18].

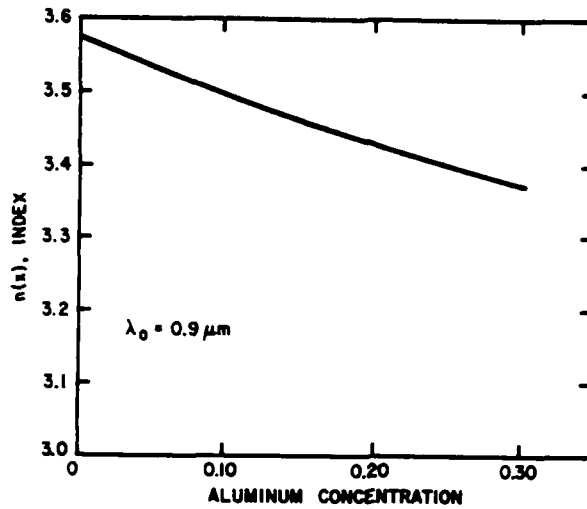


Figure 3. Index of Refraction n of $\text{Ga}_{1-x}\text{Al}_x\text{As}$ as a Function of Al Concentration.

The curve in Figure 3 is a plot of the empirically determined Sellmeier equation [18] which gives refractive index as a function of Al concentration and wavelength.

$$n^2 = A(x) + \frac{B}{\lambda_0^2 - C(x)} - D(x) \lambda_0^2 \quad (1)$$

where x is the atomic fraction of Al in the $\text{Ga}_{1-x}\text{Al}_x\text{As}$, and the constants A , B , C , and D are functions of x as given in Table 1.

TABLE 1. SELLMEIER EQUATION COEFFICIENTS (FOR λ_0 in μm)

MATERIAL	A	B	C	D
GaAs	10.906	0.97501	0.27969	0.002467
$\text{Ga}_{1-x}\text{Al}_x\text{As}$	$10.906 - 2.92x$	0.97501	$(0.52886 - 0.735x)^2$ $x \leq 0.36$ $(0.30386 - 0.105x)^2$ $x \geq 0.36$	$[(0.002467)(1.41x + 1)]$

2.1.2 Refractive Index of Quantum Well-Superlattice Composed of GaAs/AlAs or GaAs/AlGaAs

As mentioned earlier, the optical properties of a superlattice will be controlled by the quantum properties of the periodic structure in the associated system of layers. An experimental and theoretical explanation of these effects, relative to the refractive index, is presented by Suzuki and Okamoto [19] and by Kahen and Leburton [20]. These authors show that the main difference between the index of refractions of a superlattice and its corresponding AlGaAs alloy is attributable to the presence of quantized energy level transitions in the superlattices such that the difference is maximized when the energy of a transition corresponds to the frequency of light being used for the measurement. Figure 4 shows calculations of the index of refraction $n(\omega)$ of GaAs-AlAs superlattices as a function of their structure. In Figure 5 is a comparison of experimental and theoretical data on refractive index as a function of energy (eV) for a well width of 27Å and barrier width of 62Å. The results compare favorably with only minor discrepancy. In view of the favorable comparison in Figure 5 between theory and experiment the computational results in Figure 4 can be interpreted with some legitimacy. As can be seen in that figure, the superlattice refractive index is higher than the comparable bulk AlGaAs for all concentrations of Al above $x = 0.2$. The difference increases for increasing x . The difference is seen to be even greater for light polarized perpendicular to the superlattice compared to the parallel polarization state. It is clear from this figure that 2% changes in refractive index n are probable under conditions where the light moves from a superlattice media into a bulk alloyed material of comparable aluminum concentration. Changes in n of this amount are sufficient for fabricating DFB gratings under conditions where a large number of lines can be used and the line width is such as to represent a lower order index grating.

2.2 ION MIXING FOR CHEMICAL DISORDERING

A region in the vicinity of a sharp interface between AlGaAs/GaAs can have its optical properties modified by either producing a chemical mixing of the Al from the AlGaAs or else

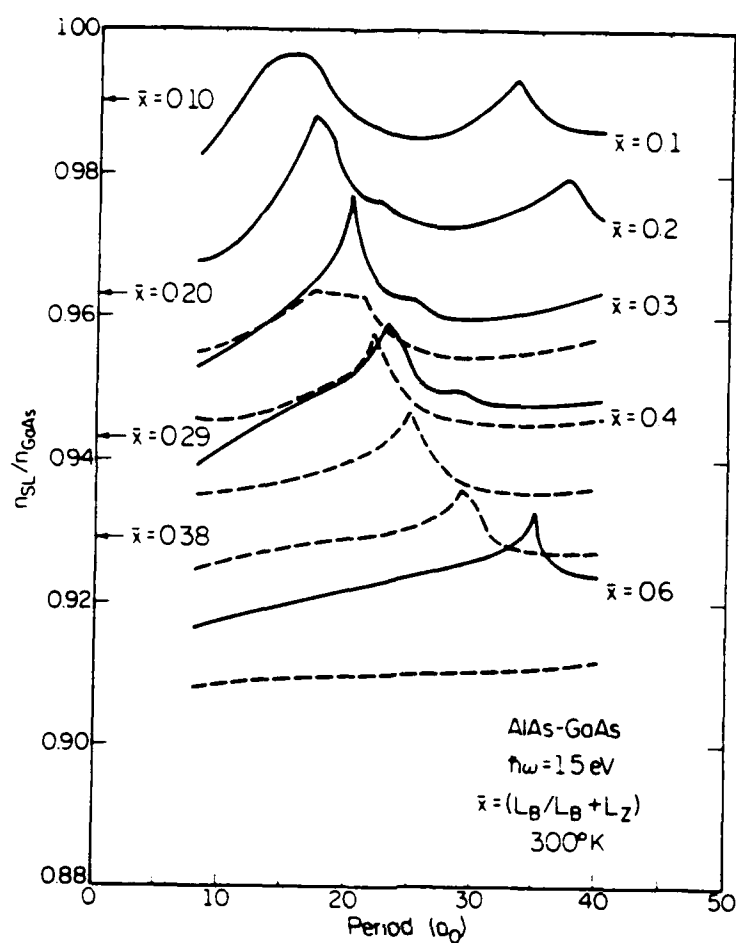


Figure 4. Index of Refraction $n(\omega)$ for GaAs-AlAs Superlattices as a Function of their Structure.

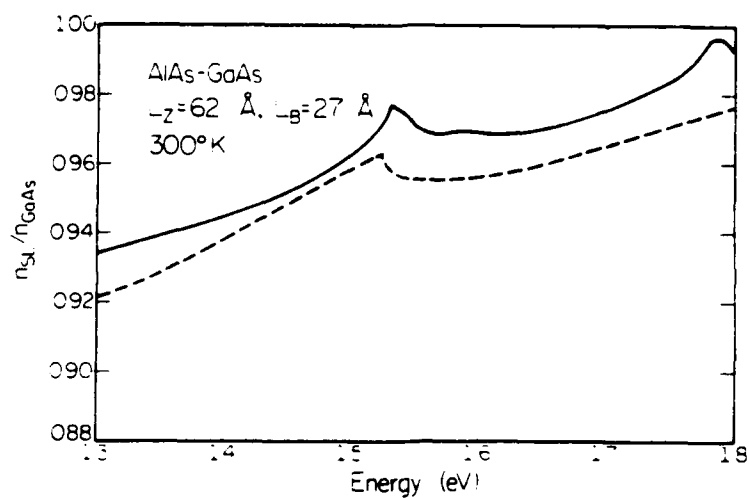


Figure 5. Comparison of Experimental (Dashed Line) and Theoretical (Solid Line) Data on Refractive Index as a Function of Energy (eV).

by introducing radiation damage or amorphizing the crystal structure of that region. In the past, chemical mixing has been introduced by Zn diffusion in these hetero-epitaxial systems [21]. In addition, ion implantation of Zn or Si has resulted in chemical interdiffusion of Al after annealing the implantation damage. This process presumably resembles a diffusion phenomena in that the chemical species Zn or Si is used as a site location disordering agent.

Our experiments rely on the implantation of chemical disordering species as well as collision cascade structural disorder. Ion irradiation is used to produce mixing of the components of the system. This process, ion beam mixing, results in the AlGaAs/GaAs material becoming amorphous under certain irradiation conditions. The amorphous material will have an index of refraction and absorption coefficient that is very different from the crystalline material. This effect in itself could be used for index light guiding or DFB operation. However, under annealing the amorphous zone will recrystallize epitaxially from the crystalline material around it (by solid phase epitaxial growth) converting the mixed zone back to crystalline material. This recrystallized material will be chemically mixed and of a crystal quality that depends on the annealing temperature. Its optical properties will be a consequence of these effects. Our intention has been to use ion implantation doping with associated diffusion under annealing and ion beam mixing with associated furnace and rapid thermal annealing to produce the necessary changes in optical index of refraction for the distributed feedback devices.

3.0 OPTICAL PROPERTIES OF MULTIPLE QUANTUM WELL ARRAYS AND THEIR RELATION TO DFB LASER DESIGN

3.1 INTRODUCTION

The application of quantum well structures to semiconductor lasers has led to improved performance and unique characteristics over the conventional double heterostructure laser. Wavelength selectivity, lower threshold current density, and better noise properties and modulation characteristics are some of the improved characteristics gained by the use of quantum

well structures. The modified density of states and quantized energy levels of the quantum well heterostructure are the main contributors to the improved performance.

All of the samples studied in this work were grown by molecular beam epitaxy (Varian 360) on undoped, (100) orientation substrates. The basic structure, as shown in Figure 6, was grown as follows. First a GaAs buffer was grown at a temperature of 627°C, and then the following layers were grown at a temperature of 640°C: $\text{Al}_x\text{Ga}_{1-x}\text{As}$ $\sim 1\text{ }\mu\text{m}$, GaAs quantum well $\sim 300\text{Å}$, GaAs/ $\text{Al}_x\text{Ga}_{1-x}\text{As}$ superlattice with $\sim 50\text{Å}$ wells and barriers (period $\sim 100\text{Å}$) or $\sim 35\text{Å}$ wells and barriers (period $\sim 70\text{Å}$), and a GaAs cap layer $\sim 500\text{Å}$. The total superlattice thickness was approximately 2000Å or 4000Å, depending on the sample. The Al composition, x , was approximately 30%.

The superlattice is to be implanted from the top surface using masking to "write" thin stripes on the order of 2000Å with the implant penetrating the thickness of the superlattice. The implantation will create regions of disordered superlattice, as shown in Figure 7, and the change in the index of refraction from the ordered to the disordered sections will result in partial reflections of the optical wave enabling distributed feedback. Given the straggle and the damage from the ion implantation, a DBR laser would most likely be the best configuration (in contrast to the DFB) in order to keep the GaAs active region free from damage.

The quantum well active region is $\sim 300\text{Å}$; narrow enough to achieve quantum effects but wide enough to keep the emission wavelength near the GaAs band edge and also wide enough to achieve some optical confinement. The evanescent wave traveling outside of the active region interacts with the grating. The Al composition of 30% to 35% gives a "nice" barrier height and dielectric step at the interfaces. The potential well is deep enough such that the carriers cannot easily escape thermally, and it is shallow enough such that not many electrons are lost to the indirect X and L bands.

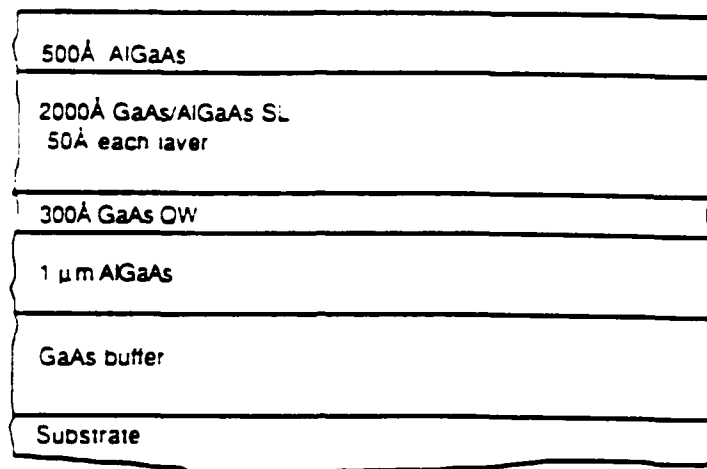


Figure 6. Schematic Diagram of the GaAs/AlGaAs Superlattice and Quantum Well Laser Structure.

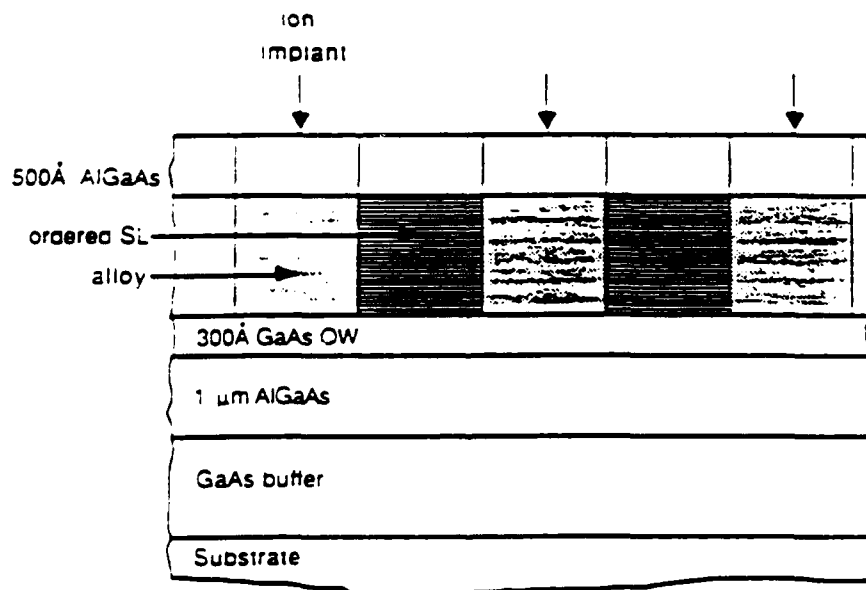


Figure 7. Schematic Diagram of the Implanted Superlattice Forming a Grating for Distributed Feedback.

Note that this is an unsymmetric double heterostructure, the thick $\text{Al}_{0.3}\text{Ga}_{0.7}\text{As}$ cladding layer provides a larger barrier and a larger dielectric step than the superlattice. The optical wave, therefore, will penetrate further into the superlattice than into the $\text{Al}_{0.3}\text{Ga}_{0.7}\text{As}$ cladding layer allowing for the interaction with the grating. The 50Å or 35Å wells in the superlattice allow for good coupling between the wells and reasonable thicknesses for the crystal growth.

3.1.1 Multi-Quantum Well/Superlattice Material Fabricated by Molecular Beam Epitaxial Crystal Growth

All material evaluated in this program was fabricated by Molecular Beam Epitaxy (MBE) in a Varian 360 MBE system located at the Electrical Engineering Department of North Carolina State University. This system, which includes a preparation and evaluation chamber, has the following features:

- Ultra-high vacuum (UHV) system which is capable of producing a background pressure in the 10^{-11} torr range.
- Work chamber for epitaxial growth which permits substrate heating and manual rotation. Two substrate holders are provided in the working chamber.
- Source flange which connects to the work chamber and has provisions for mounting eight source furnaces, furnace shutters, and liquid nitrogen cooled baffles. Presently, the eight source furnaces contain Al(1), Al(2), Ga, In, As, Sb, Si, and Be.
- Sample preparation chamber which permits pre- and post-deposition and analysis of specimen, provides for UHV "storage" of six substrates or specimens, has extra posts for mounting additional sample treatment devices and analytical components, and provides for transfer of substrate/specimen into and out of the deposition chamber without loss of UHV.
- Substrate heater with a temperature range of 200°C to 700°C with regulation of $\pm 0.5^\circ\text{C}$ at 700°C.

- Double-load-lock system which permits removal of grown wafers from the system and insertion of new substrates into the sample preparation chamber without loss of UHV conditions in the sample preparation chamber.
- Bakeout capabilities of 200°C for the total UHV system.
- Metal seals on all valves associated with the growth chamber.
- Source furnaces with inside dimensions of 0.92 inch in diameter by 5.88 inches long with a temperature stability of $\pm 0.5^\circ\text{C}$ at 1200°C over 24 hours.
- Microprocessor-controlled shutters for all eight furnaces to allow reproducible and consistent thin-layer structures.

In addition to the basic MBE 360 system with the added preparation chamber, the following analytical capabilities are part of the system:

- Beam flux monitor gauge (ionization gauge) which can be rotated on the work chamber carousel to the same position as the substrate holder for measuring the same flux as that "seen" during growth.
- Reflection electron diffraction (RED gun) system capable of deflecting up to a 10 keV beam of electrons over the surface of the substrate.
- Quadrupole mass spectrometer located near the substrate in the main chamber capable of 0 to 300 amu. In addition, this system is capable of use in an expanded mass scale with unit mass resolution.
- Sputter-Auger scanning spectrometer capable of determining elemental composition of surface up to 10-30Å. This system, mounted in the preparation chamber, includes an ion bombardment gun for depth-profiling applications.

The sections immediately following this one discuss the measured optical properties of quantum well-superlattice material fabricated in this system. A full materials evaluation and characterization of such samples is presented starting in Section 4.0.

3.2 SPONTANEOUS PHOTOLUMINESCENCE OF THE MBE MATERIAL

The layer thicknesses and Al composition can be confirmed by photoluminescence (PL) spectroscopy. Generally, emission resulting from the recombination of the lowest energy states ($n=1$ for electrons and heavy holes) can be readily identified on the PL spectra. It is customary to denote electron to heavy hole transitions as $n=1, 2, \dots$ and to denote electron to light hole transitions as $n=1', 2', \dots$. The superlattice (SL) and quantum well (QW) peaks are usually very clear on the spectra and the emission wavelengths vary as a function of layer thickness and composition. The Al composition can be determined from the platelet (substrate removed) PL, as there is usually a small emission peak from the $1 \mu\text{m Al}_x\text{Ga}_{1-x}\text{As}$ layer. The emission energy from this relatively thick (bulk-like) layer is compared with the $\text{Al}_x\text{Ga}_{1-x}\text{As}$ bulk band gap which is well characterized as a function x .

The spontaneous emission at 77K from three samples is compared in Figure 8 and Figure 9. Rectangles a few millimeter on a side were cleaved from the as-grown wafers, pressed into In, and photopumped with an argon ion laser (5145\AA). The emission peak in the 7500\AA to 7900\AA range is from the SL and the peak at approximately 8200\AA is from the QW. The $n=1$ and $n=1'$ transitions have been calculated using a finite square well model, and they are shown in the figures with dark markers and light markers, respectively. The position of the SL peak is dependent on the layer thicknesses and the Al composition. The peak is at higher energy for thinner layers. The confined particle transition energies were calculated with the following input parameters: curve (a) 260\AA QW plus SL region with 30\AA wells and barriers, $x=0.32$; curve (b) 350\AA QW plus SL region with 35\AA wells and barriers, $x=0.31$; and curve (c) 350\AA QW plus 55\AA layers in the SL, $x=0.28$. The thicknesses agree with crystal growth rates and times. The total thicknesses of the SL regions were as follows: curve (a) $\sim 1200\text{\AA}$, curve (b) $\sim 3580\text{\AA}$, and curve (c) $\sim 4400\text{\AA}$.

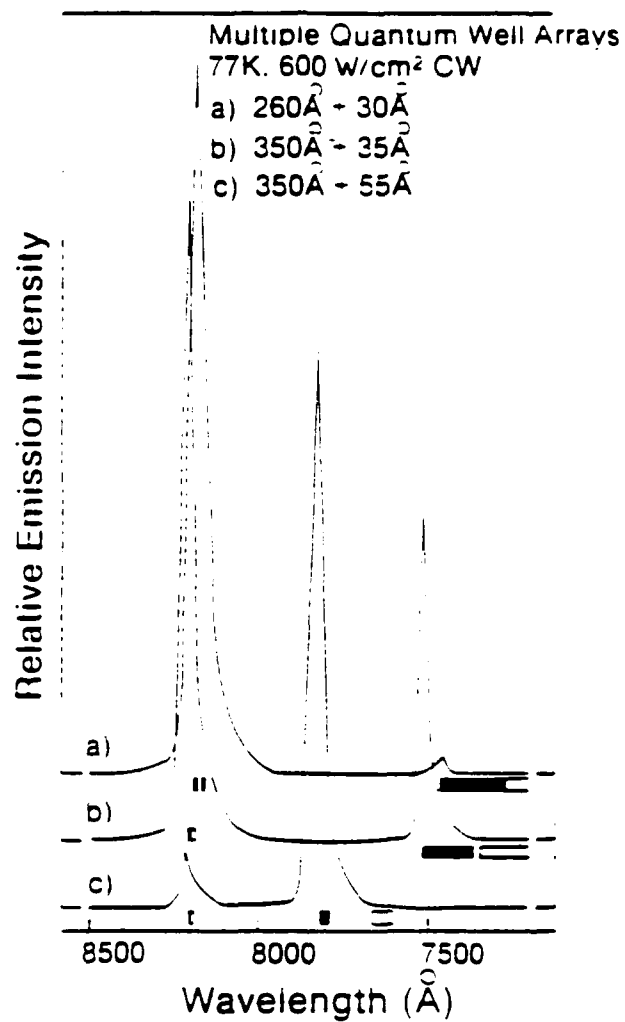


Figure 8. Spontaneous Emission from Three Different Quantum Well/Superlattice Samples with Different Layer Thicknesses.

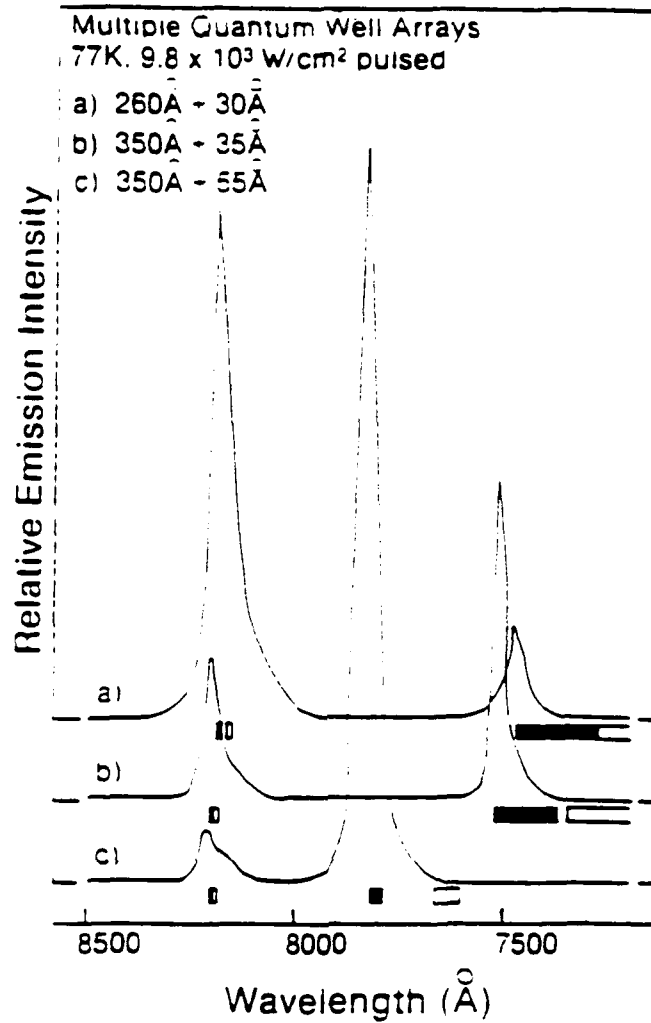


Figure 9. Spontaneous Emission from the Samples of Figure 8 at Higher Pumping Power.

In Figure 8, using a relatively low power CW pumping level of 600 W/cm^2 , curves (a) and (b) are dominated by the QW emission signifying efficient carrier collection by the QW. In curve (c), however, the emission is dominated by the SL. At a higher excitation level ($9.8 \times 10^3 \text{ W/cm}^2$ pulsed, 3.8 MHz), as shown in Figure 9, the SL intensity increases relative to the QW peak. Note that for curve (a) the QW is still larger. At even higher power levels, this sample continues to show efficient collection by the QW. The QW peak broadens and develops a broad shoulder at $n=2$ indicating band filling. This is an important effect considering that high power densities are utilized in laser diodes.

The relative intensities are not simply dependent on the total SL thicknesses since additional samples were examined in which the total thicknesses varied. The emission appears to be dependent on the individual layer thicknesses and the resulting energy levels in the structure.

This effect of SL versus QW emission dominating the spectra is examined more closely in the following section. Given that the total thickness of the SL is larger than the QW and that the sample is excited from the top surface, many more carriers are generated in the SL region than in the QW region. If the allowed energy levels of the two regions overlap such that the carriers can tunnel to the QW from the SL, then the QW emission can be quite large even though the carriers are not generated in that region. With higher pumping power and greater carrier generation, the transport to the QW can saturate leaving more carriers to recombine in the SL region, and thus the relative peak intensities would show a power dependency.

Since the QW is to be the active region in the device, it is desirable that the carriers reach the QW and recombine there, as opposed to being collected in the SL region. In order to sustain laser operation in the QW, enough carriers need to be collected such that population inversion is achieved. As will be shown in a later section, there is a correlation between the samples with a large spontaneous QW emission and a lower QW lasing threshold.

3.3 COUPLING OF ENERGY LEVELS BETWEEN THE SL AND QW

The energy band diagram is modeled by a series of potential wells for electrons (conduction band) and holes (valence band) as shown in Figure 10. For illustrative purposes, the superlattice region is shown as only five thin wells. In the superlattice region, the closely spaced energy levels form mini-bands, whereas in the large well, there are discrete energy levels. If the energy levels from the large quantum well line up with a mini-band, then efficient tunneling can occur from the superlattice to the quantum well where the carriers can then thermalize to lower energy states and recombine.

When the SL and the QW are considered as two separate entities, each has distinct energy levels which depend on the barrier height, well thickness, and the percent of the total band gap discontinuity in the conduction band. However, when the two are brought close together, the wavefunctions interact and any degenerate or near-degenerate energy levels split and the wavefunction spreads out in the two regions. If the energy levels do not overlap, then there is little interaction and the wavefunction remains localized in the QW or SL, respectively. Although the tunneling probabilities were not calculated explicitly, the spatial extent and the amplitude of the wavefunction gives an indication of the amount of tunneling that can occur in the structure.

When the energy levels are considered for the samples in Figures 8 and 9, it is found that the overlap is very good for sample (a) with the strong QW emission, the overlap is less for sample (b), and even less for the sample (c) with the strong SL emission. The energy levels are shown in Figure 10 for sample (a) and Figure 11 for sample (c). Since the QW is rather large there are many closely spaced energy levels, especially for the heavy holes. The SL mini-bands spread out in energy for the thinner layered sample and only five energy levels are shown since five coupled wells were used as an approximation to the superlattice in the actual sample. Larger number of wells were also used to approximate the SL, and it was found that the mini-band did not spread out in energy significantly when compared to the five well approximation.

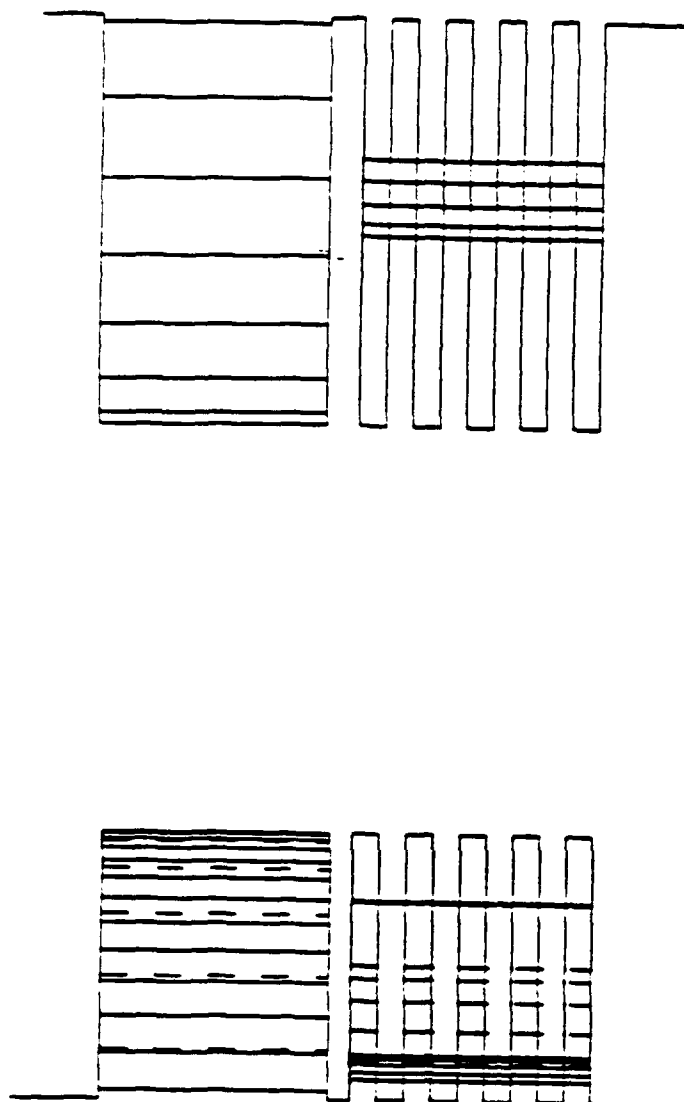


Figure 10. Energy Band Diagram for the Multiple Quantum Well Array. Large QW = 260\AA ; SL with 30\AA Wells and Barriers.

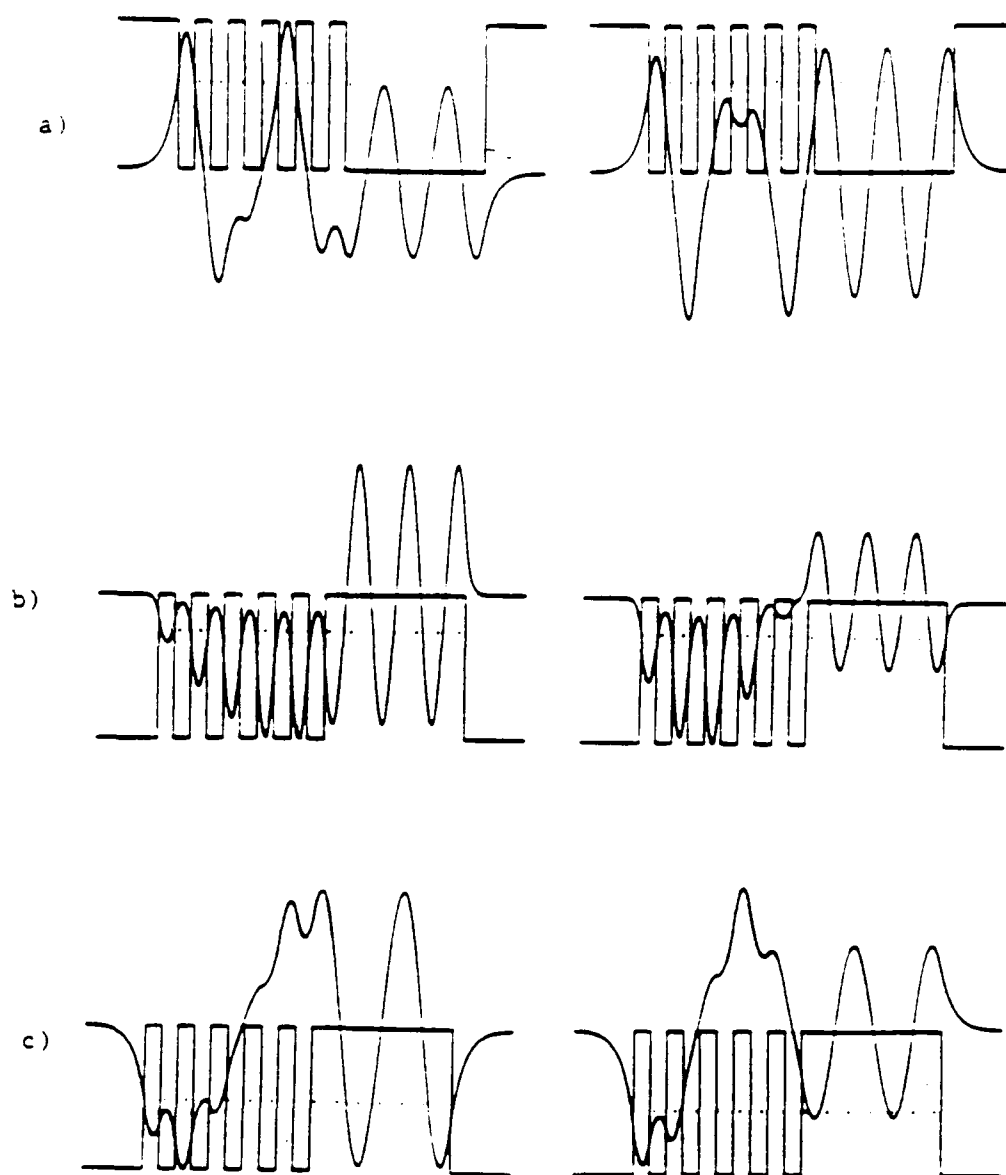


Figure 11. Selected Wave Functions for the Potential of Figure 10.

First consider the sample with the thinner wells and barriers in the SL ($\sim 30\text{\AA}$) and the $\sim 260\text{\AA}$ large QW, as shown in Figure 10. In the diagram, increasing electron energy is upward and increasing hole energy is downward. The conduction band discontinuity is 239 meV and the valence band discontinuity is 160 meV, as calculated by $\Delta E_c = 0.6\Delta E_g$ and $\Delta E_v = 0.4\Delta E_g$ where ΔE_g is found for GaAs/ $\text{Al}_{0.32}\text{Ga}_{0.68}\text{As}$.

The energy levels of all three carriers overlap effectively in this sample. The SL $n=1$ electron bound state (or mini-band) couples with $n=5$ state of the QW. The SL $n=1$ heavy hole state has nearly the same energy as the QW $n=6$ heavy hole state. And both the $n=4'$ and $n=5'$ QW light hole states overlap with the SL $n=1'$ light hole mini-band. The carriers collected in the SL region can tunnel to the QW, thermalize to lower energy bound states and recombine.

Wavefunctions of selected energy levels for this potential (Figure 10) are shown in Figure 11. The wavefunctions shown represent the overlapping energy levels, and the wavefunctions spread out effectively for all carriers: (a) electrons, (b) heavy holes, and (c) light holes. For the heavy holes, the QW bound state is slightly lower in energy than the SL state, but the energy levels appear to couple very well. In the higher energy SL states of the mini-band (not shown), the amplitude of the wavefunction progressively decreases in the QW region.

Ideally, the QW states should line up with the bottom of the SL mini-band since the carriers in the SL will thermalize to the bottom of the band. Even if the states do not line up exactly, tunneling can still occur due to the thermal energy (kT) of the carriers if the QW state has slightly lower energy than the SL states.

Now consider the sample of Figure 12, in which the energy levels do not overlap nearly as well. In this sample, the SL layers are thicker ($\sim 55\text{\AA}$) and the large QW is $\sim 350\text{\AA}$. The conduction band discontinuity is 209 meV and the valence band discontinuity is 140 meV, as found from the 60/40 splitting of the total band gap discontinuity for GaAs/ $\text{Al}_{0.28}\text{Ga}_{0.72}\text{As}$. The SL mini-bands are quite narrow and the energy levels would have to match very closely with available states in the large QW.

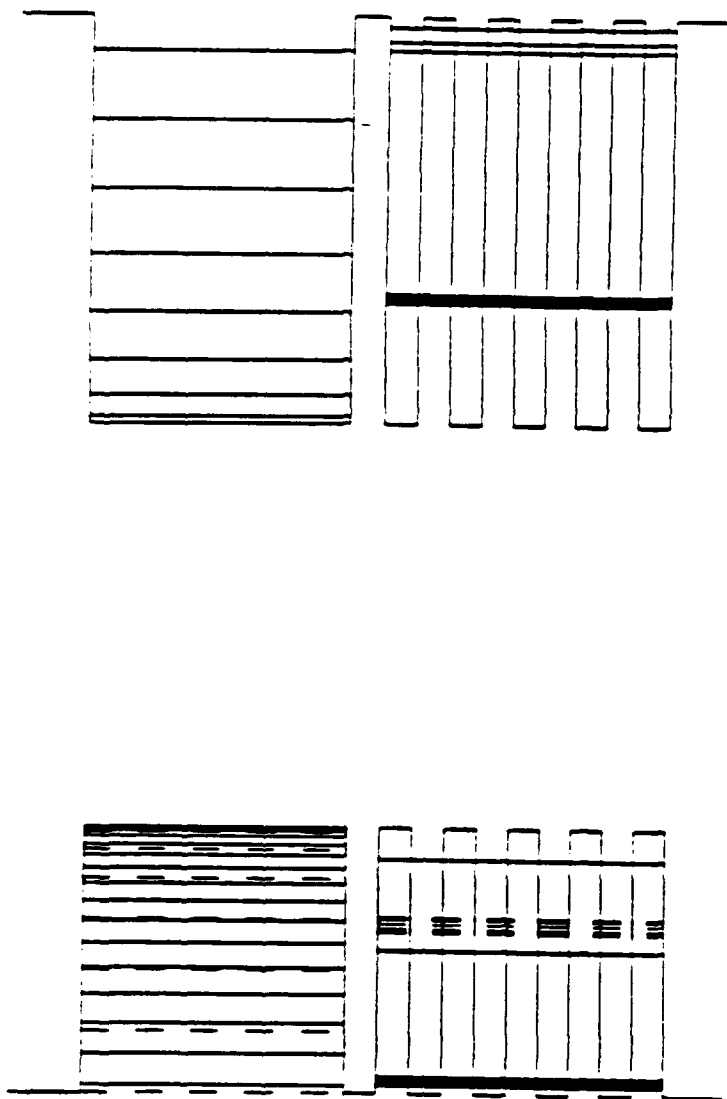


Figure 12. Energy Band Diagram for Multiple Quantum Well Array. Large QW = 350\AA ; SL with 55\AA Wells and Barriers.

The wavefunctions for the closest matched states are shown in Figure 13. The electron states do not couple well since the SL $n=1$ state is displaced in energy from available states in the QW. The SL $n=2$ state is close in energy to the QW $n=8$ state, however, it is unlikely that the SL $n=2$ state is populated since it is at a much higher energy than the SL $n=1$ state. Even though the heavy hole states are very close in energy (~ 1 meV displacement), the wavefunctions show very little, if any, overlap. This can be seen in Figure 13(b) where the wavefunction is localized in one region or the other. The light hole energy levels couple well, as the SL $n=1'$ and QW $n=4'$ levels overlap. In general, the electron and light hole states couple more effectively than the heavy hole states for the same energy displacement due to the smaller effective mass.

This coupling, or tunneling, effect could very well be responsible for the striking differences in the PL spectra of these two samples. The other sample shown in Figure 8 with the $\sim 35\text{\AA}$ SL layers and a $\sim 350\text{\AA}$ QW, exhibited fairly good electron and light hole coupling, with less heavy hole coupling. And accordingly, the PL spectra was not as marked as in the other two samples. Since the energy levels shift with the layer thicknesses, it is very important to control the thickness of the large QW layer in particular, in order to achieve the degenerate energy levels needed to achieve efficient carrier collection and recombination in the QW.

3.4 PHOTOPUMPED LASER OPERATION

Small Fabry-Perot cavities were made from the samples by removing the substrate and cleaving the epi-layer into rectangles 20 to 50 μm in width by 100 to 400 μm in length. The platelets are then pressed into indium under a sapphire window. The samples were photopumped at 77K with an argon laser (5145\AA) focusing the beam to approximately 30 μm in diameter.

All of the samples were of laser quality, supporting stimulated emission in the superlattice and the quantum well regions. The threshold powers were fairly average for samples prepared in this way. As the power intensity of the pumping laser is increased, the emission from the

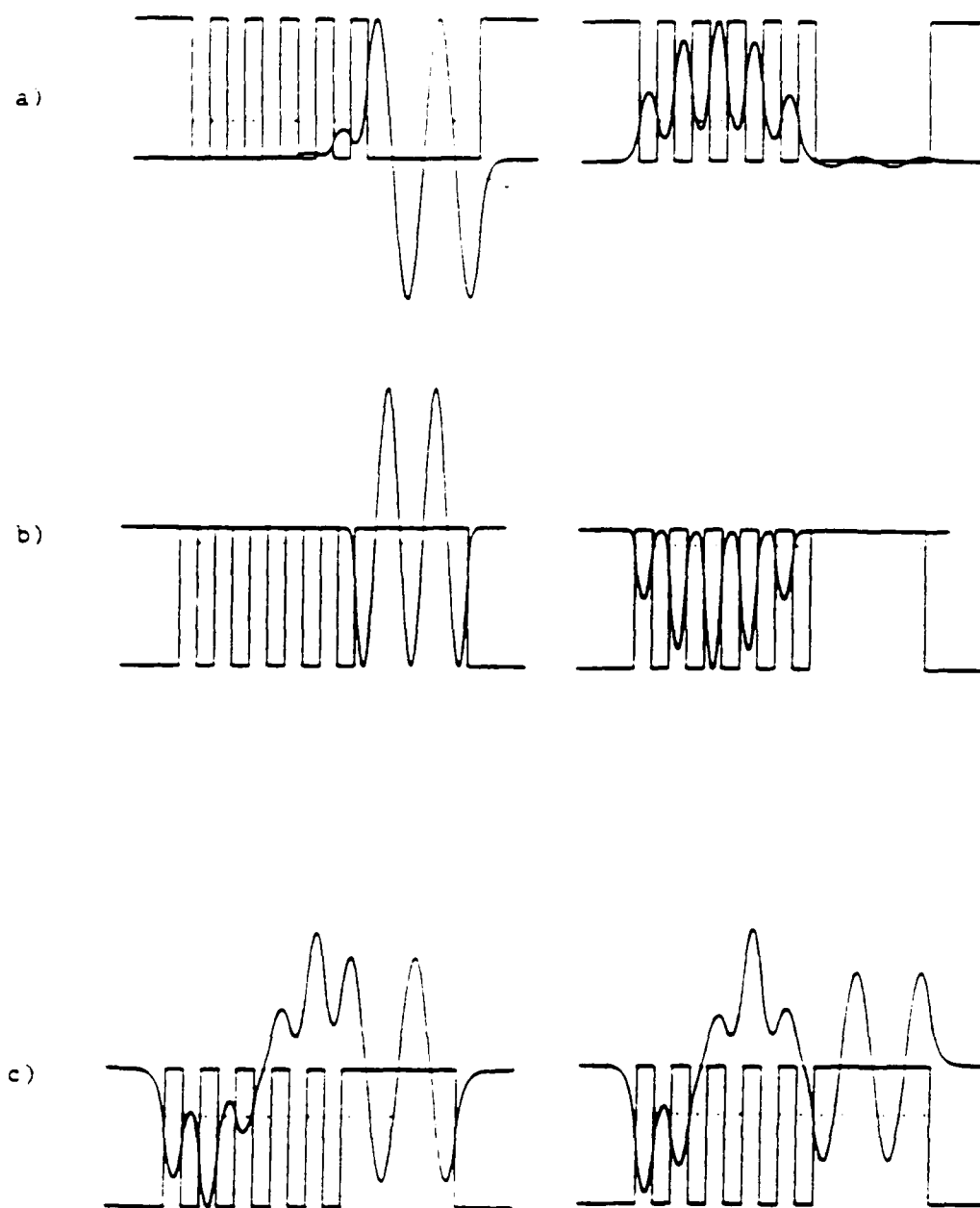


Figure 13. Selected Wavefunctions for the Potential of Figure 12.

platelet changes from spontaneous to stimulated emission. The threshold power is taken to be the pumping power at the onset of laser modes in the emission spectra. 75% of the measured power was used as a conservative estimate for the power loss at the mirrors, focusing lens, dewar window, and the sapphire window.

For samples with thicker SL layers (55Å to 60Å) where the tunneling effect was not as prominent, the lasing was primarily in the SL. A typical platelet spectra is shown in Figure 14. The lasing modes appear on the low energy side of the peak since the absorption losses are lower for those energies. The threshold power for this sample is 3.1×10^4 W/cm². Note the ringing (i.e., weak Fabry-Perot modes) in the QW region. The oscillatory behavior indicates that there are standing waves but that the gain cannot overcome the losses as lasing is not achieved even with higher pumping power.

The lasing modes in the SL are spaced one LO phonon energy ($\hbar\omega_{LO} \approx 36$ meV) below the electron to light hole transition. Since the light hole and heavy hole states are displaced by ~ 29 MeV, it is difficult to know with certainty whether the lasing is due to phonon-assisted stimulated emission or whether the lasing occurs on the long wavelength side of the $n=1$ SL transition due to high optical losses. Phonon-assisted lasing has, however, been reported [22-24] by various researchers in a variety of structures. The mode spacing indicates that the lasing cavity length is across the width of the platelet ($\Delta\lambda = \lambda^2/2nL$, where $\Delta\lambda$ is the mode spacing, λ is the lasing wavelength, n is the effective index of refraction, and L is the cavity length). Researchers have found that phonon-assisted stimulated emission generally runs in the length of the sample since the absorption losses are low for the lower energy emission. In this case, however, the absorption losses would not necessarily be lower in the long direction due to the GaAs QW.

For samples with thinner SL layers (30Å to 35Å) and better coupling between the SL and QW regions, the lasing most often occurred in both regions. The platelets for these samples showed lasing mainly in the QW, and the QW usually had a lower threshold power than the SL. From the finite square well model, it appeared that the combination of Al composition and layer

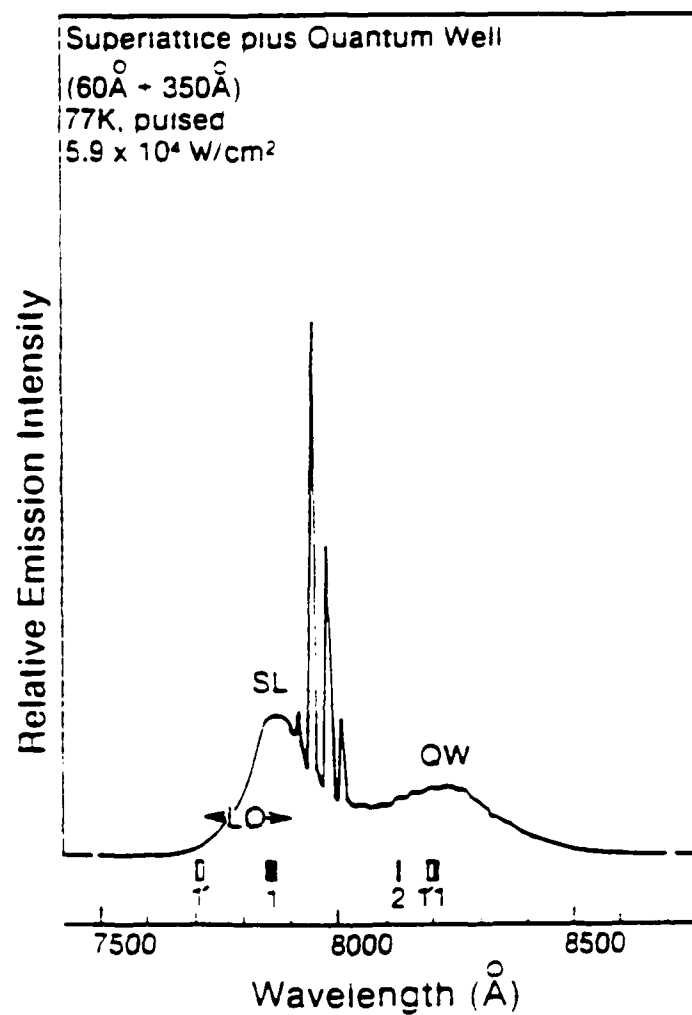


Figure 14. Stimulated Emission for a Typical Platelet ($24 \mu\text{m} \times 258 \mu\text{m}$) with 60\AA SL Layers and a 350\AA QW.

thicknesses for these samples was conducive to carrier tunneling from the SL to the QW allowing for enhanced carrier collection in the QW. In this case, stimulated emission can be supported in the QW since enough carriers are collected to achieve population inversion.

The spectra shown in Figure 15 is from a platelet ($44\text{ }\mu\text{m} \times 255\text{ }\mu\text{m}$) with 30\AA SL layers and a 260\AA QW. The QW lases first ($P_{\text{th}} = 8.7 \times 10^3\text{ W/cm}^2$) as the pumping power is increased, followed by the SL ($P_{\text{th}} = 2.4 \times 10^4\text{ W/cm}^2$), and modes appear between the two energy levels. These modes are spaced $2\hbar\omega_{\text{LO}}$ below the SL peak. They are also very close to the $n=3$ transition for the large QW. These modes could be a result of band filling in the large QW and lasing on the $n=3$ transition, or they could be a result of phonon-assistance below SL $n=1$ transition.

Another example is shown in Figure 16 (30\AA SL layers and a 260\AA QW). In this sample, the lasing occurs on the QW $n=1$ transition (not shown, $P_{\text{th}} 1.0 \times 10^4\text{ W/cm}^2$) and then the lasing shifts to the $n=2$ transition at increased power levels. Sustaining laser operation at higher energy levels in the QW demonstrates band filling and efficient carrier collection. The lasing modes $2\hbar\omega_{\text{LO}}$ below the SL transition also coincide with the $n=3$ QW transition, however, the abrupt turn-on and the absence of a spontaneous peak is indicative of phonon-assisted stimulated emission. In the following section, when the SL peak is shifted through annealing, emission is still evident $2\hbar\omega_{\text{LO}}$ below the SL transitions supporting the conjecture of phonon-assisted stimulated emission.

The emission spectra of a sample with only a superlattice region and no large QW (35\AA wells and 35\AA barriers, $x=0.27$) is shown in Figure 17. In this structure, the light and heavy hole bands are displaced by $\sim 29\text{ meV}$. The lasing modes appear ($P_{\text{th}} = 5.2 \times 10^4\text{ W/cm}^2$) very near the $n=1$ transition, and incidently they are spaced 36 meV below the $n=1'$ transition. The peak is well defined, and no low energy emission is observed. This indicates that the SL layers are of high quality since no cluster-induced tail [25] is observed. Clusters of GaAs and/or AlAs in the barrier regions have been reported to create states below the expected transition level resulting in a long tail in the emission peak [25]. Assuming the other samples, which were grown under

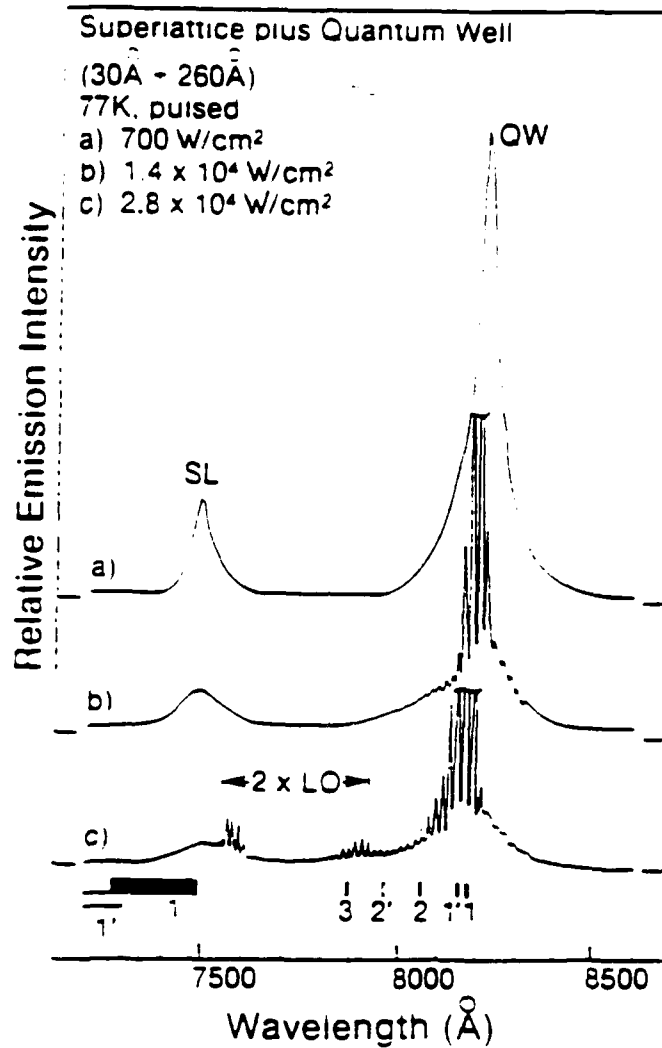


Figure 15. Stimulated Emission for a Platelet (44 μm × 255 μm) with 30Å SL Layers and a 260Å QW.

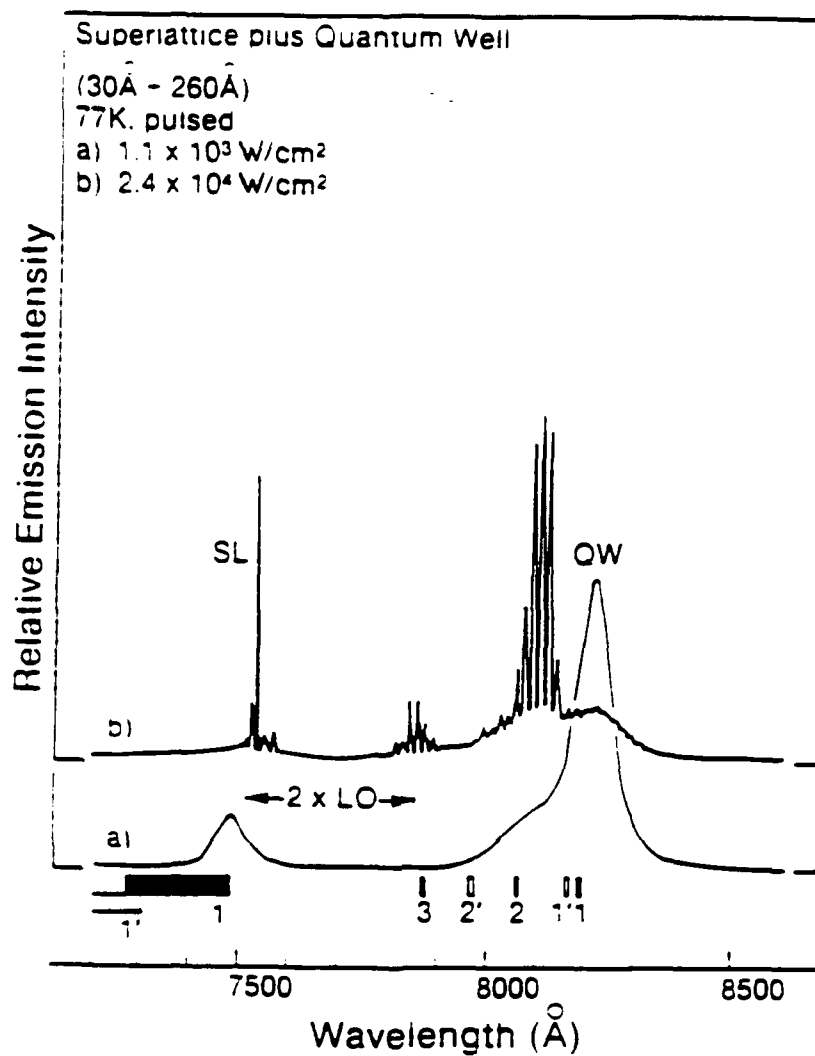


Figure 16. Stimulated Emission for a Platelet ($41 \mu\text{m} \times 415 \mu\text{m}$) with Same Structure as Figure 15.

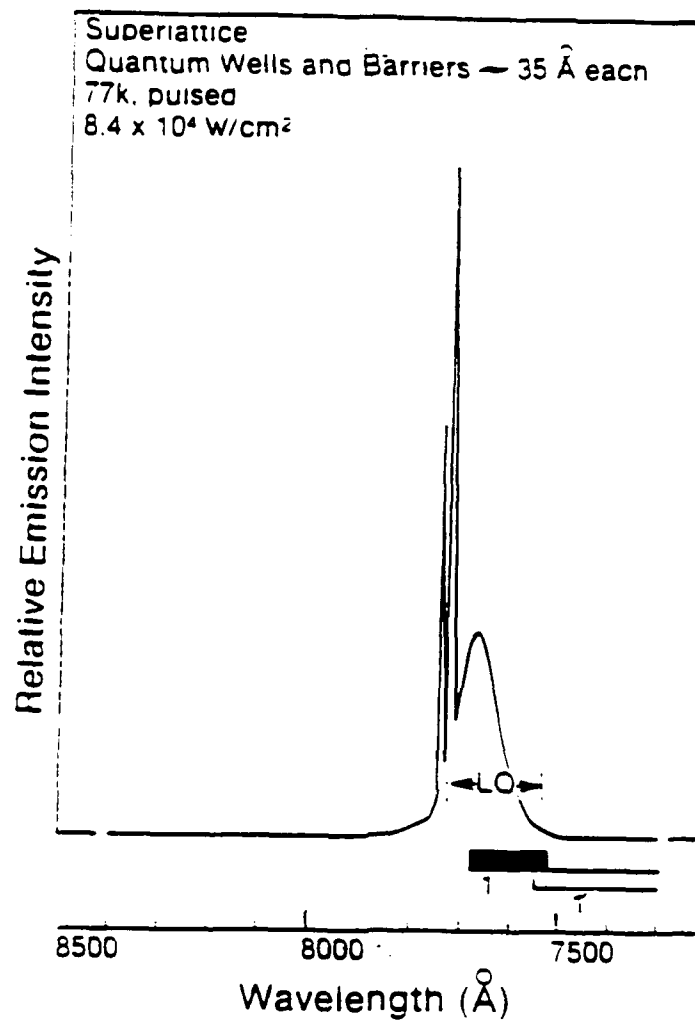


Figure 17. Stimulated Emission for a Platelet ($32 \mu\text{m} \times 133 \mu\text{m}$) with SL Region only and no QW.

similar conditions, are also of such quality, the transition observed between the SL and QW energies are most likely not a result of cluster-induced states or donor/acceptor states.

3.5 ANNEALING OF MULTIPLE QUANTUM WELL ARRAY

Annealing was performed on two samples under various conditions to examine the stability of the structure at high temperatures. The annealing was carried out by K.Y. Hsieh in a sealed ampoule with either Ga or As over pressure for 30 minutes at a temperature of 850°C. It has been demonstrated that annealing with Ga over pressure tends to preserve the structure, whereas annealing with As over pressure tends to enhance the disordering process [26]. This phenomenon is attributed to the interdiffusion of Al and Ga via Ga vacancies.

A comparison between the as-grown structure, annealing with Ga over pressure, and annealing with As over pressure is shown in Figure 18. As expected, the emission peaks did not shift in the case of the Ga over pressure. With As over pressure, however, the SL peak is shifted by approximately 250Å and the intensity is quite low. This indicates that SL layers are beginning to intermix. The large QW remains fairly stable for this annealing time and temperature. As a result, the annealing conditions must be well controlled in order to preserve the unimplanted SL and achieve the desired effect in the distributed feedback structure.

Platelets were made from the samples annealed with As over pressure in order to examine the stimulated emission. In Figure 19, it can be seen that stimulated emission was supported by the cavity ($P_{th} = 8.6 \times 10^4 \text{ W/cm}^2$), however, the QW did not lase. Since the SL has been shifted to higher energy, it is shifted further away from the higher energy transitions of the QW. The stimulated emission occurs two phonon energies (~72 meV) below the SL $n=1'$ transition. It is interesting to note that the SL peak has been displaced substantially in energy from the QW peak, and emission still occurs multiple phonon energies below the SL $n=1$ and $n=1'$ transitions. This supports the theory of phonon interaction, as opposed to the emission simply being a result of populating the higher energy states in the large QW.

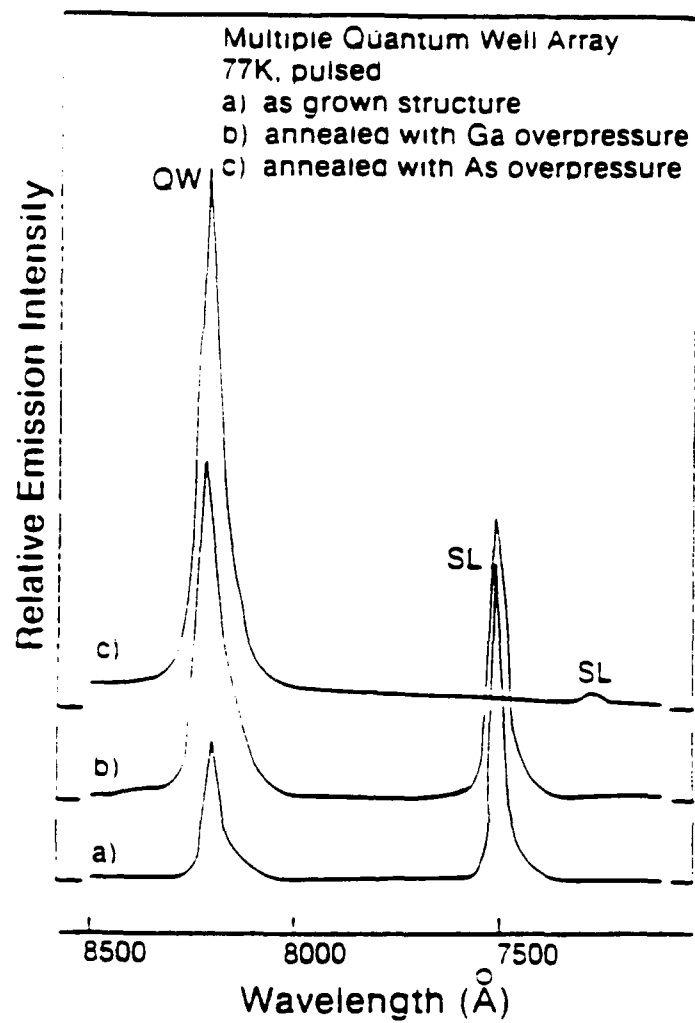


Figure 18. Comparison of Spontaneous Emission from As-Grown Sample and Samples Annealed in Ga or As Over Pressure.

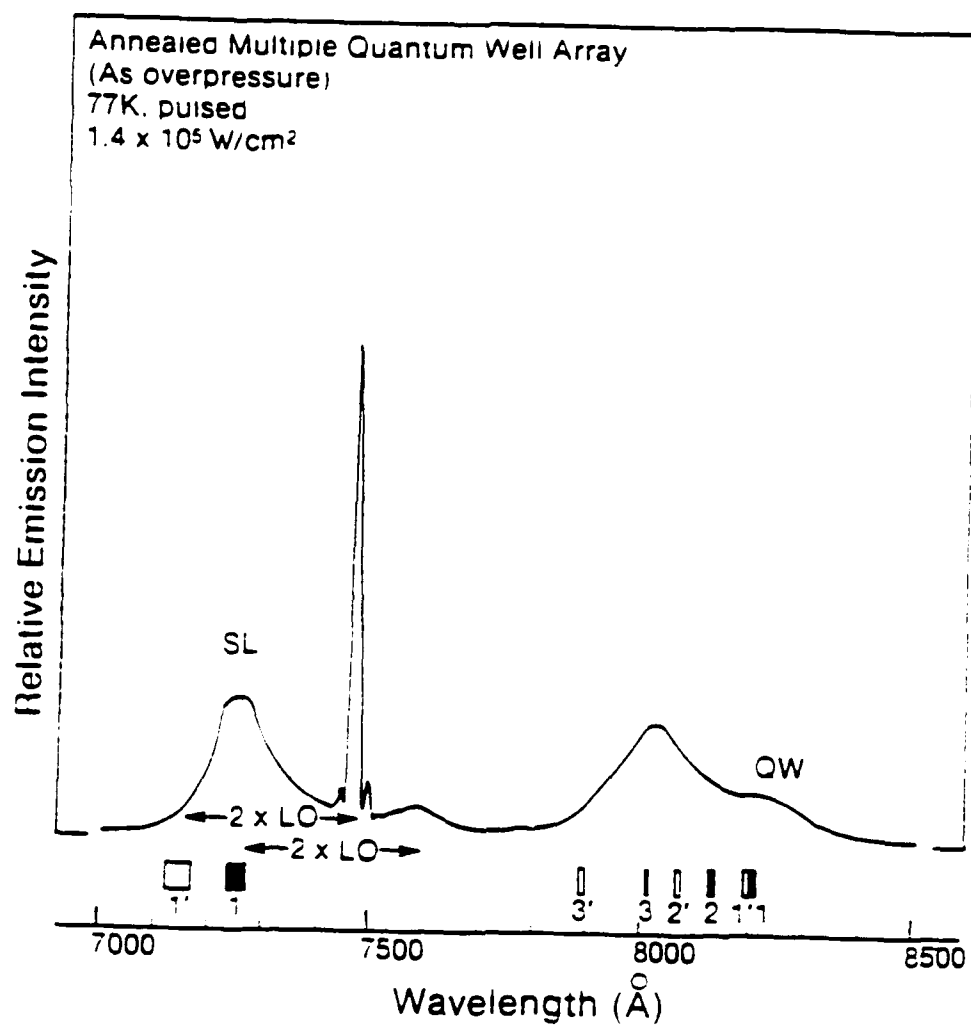


Figure 19. Platelet Spectra ($25 \mu\text{m} \times 138 \mu\text{m}$) from Sample Annealed in As Over Pressure.

The emission peak coinciding with the QW $n=3$ transition could be a result of band filling the QW since a relatively large excitation power was used. This would indicate that the QW has not been disordered significantly during the anneal.

Another example is shown in Figure 20. In this platelet, stimulated emission is never quite achieved, but substantial ringing is evident throughout a large energy range. A spontaneous peak is again located $2\hbar\omega_{LO}$ below the SL $n=1$ transition, and there is an additional peak $\hbar\omega_{LO}$ below the QW $n=1$ transition. This phenomenon of emission below the GaAs band edge has been observed before and has been attributed to phonon-assistance through virtual states [24,27].

The annealing of these structures has shown that 1) careful consideration must be given to the effects of processing and thermal cycling on the thin layers of the SL and even the QW, if lasing is to be expected in the QW region; and 2) the occurrence of emission peaks spaced multiples of $\hbar\omega_{LO}$ from the shifted SL peak is evidence of phonon interaction in this multiple quantum well array.

3.6 SUMMARY AND CONCLUSIONS OF OPTICAL PROPERTIES OF QW/SL ARRAYS

The epitaxial layers of multiple quantum well arrays were studied using photoluminescence spectroscopy to examine the spontaneous and stimulated emission. By examining the optical properties of photopumped lasers, it is possible to gain valuable information about the lasing characteristics without having to process an injection laser. The structure, consisting of a large GaAs quantum well and a GaAs/AlGaAs superlattice region, appears to be well suited for the application to a distributed feedback or distributed Bragg reflector laser in which the large quantum well is the active region, and the superlattice region is disordered in a periodic fashion by selective ion beam implantation to provide the feedback.

In order to enhance the carrier collection in the quantum well, it is desirable to couple the allowed energy levels in the SL with the bound states in the QW. By controlling the layer

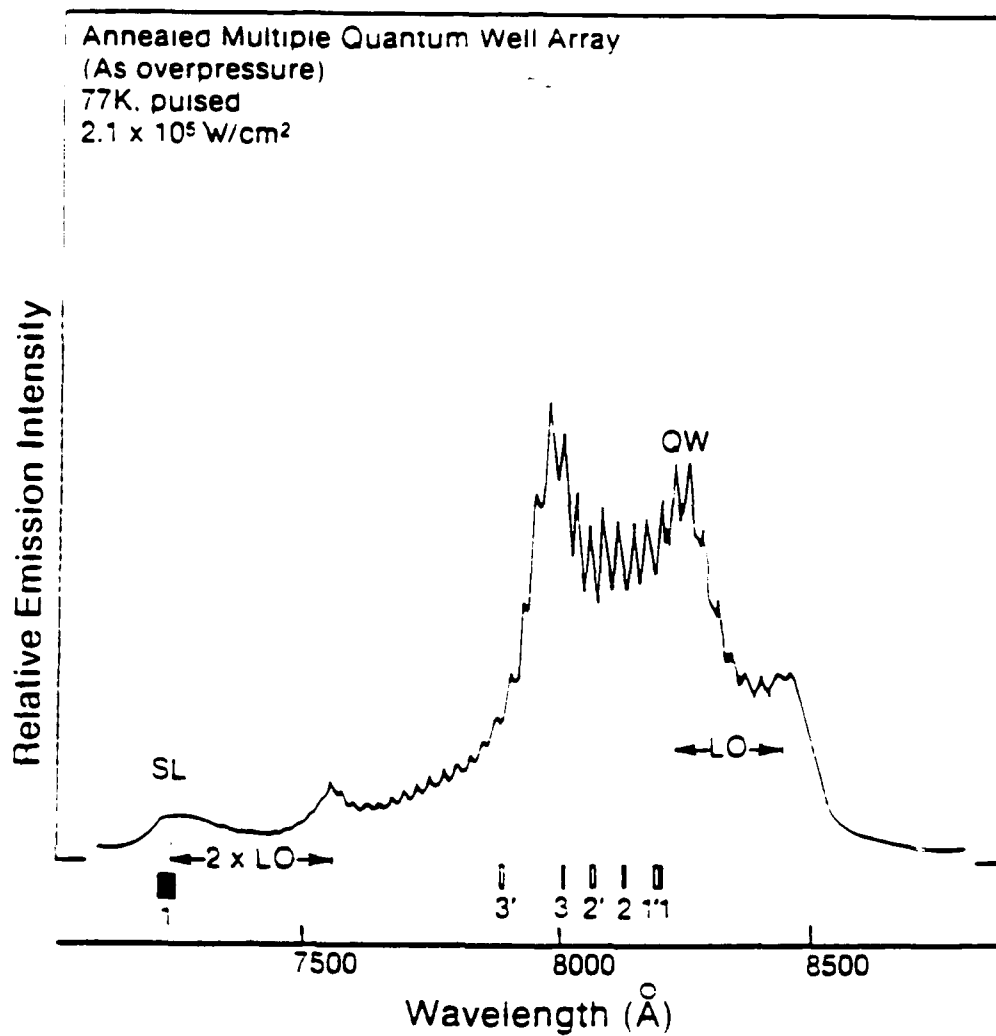


Figure 20. Emission from Platelet ($30 \mu\text{m} \times 240 \mu\text{m}$) Made from Sample Annealed in As Over Pressure.

thicknesses and the Al composition, the energy levels in the two regions can be lined up, allowing the carriers collected in the thick SL region to tunnel to the QW, thermalize to lower energy states and recombine. The SL mini-bands spread out in energy for thinner wells and barriers, and as a result, there is generally better coupling to QW bound states.

In the case of $\sim 30\text{\AA}$ SL layers, $\sim 260\text{\AA}$ QW, and $x=0.32$, a finite square well model indicated efficient coupling of electrons, heavy holes, and light holes. The photoluminescence showed a very strong QW peak, even for high pumping powers, verifying efficient carrier collection in the QW. For the case of $\sim 55\text{\AA}$ SL layers, $\sim 350\text{\AA}$ QW, and $x=0.28$, the SL mini-bands were tighter, the wavefunctions remained localized in the SL or QW regions, and the photoluminescence showed strong SL emission with weak QW emission. This tunneling, or coupling, effect is very sensitive to layer thicknesses, and therefore, in order to take advantage of the increased carrier collection, it is important to carefully control the layer thicknesses and the Al compositions during crystal growth.

Small Fabry-Perot cavities were made from the epitaxial layers in order to study the stimulated emission. There was a correlation between the overlapping energy levels as predicted by the finite square well model and the lasing threshold for the QW. When the coupling between the SL and the QW states was good, then the QW generally lased at a lower threshold than the SL. With efficient coupling, it was possible to band fill the QW and lasing was supported on higher order bound state transitions.

Laser modes were also observed $\sim 2\hbar\omega_{LO}$ below the $n=1$ SL transition. The close overlap with the $n=3$ QW transition, however, makes it difficult to know with certainty whether the lasing was due to phonon-assisted stimulated emission or whether the lasing was due to band filling. When the SL peak was shifted to higher energy as a result of annealing, spontaneous and stimulated emission was observed $\sim 2\hbar\omega_{LO}$ below the shifted $n=1$ and $n=1'$ transitions. Since these modes do not overlap with higher order QW transitions and they are multiple LO phonon energies below the SL transitions, they are best explained by phonon-assisted stimulated emission.

Considering that ion implantation and annealing is an integral part of the final laser structure, annealing with Ga over pressure and As over pressure was performed. Since the SL layers are rather thin, even short annealing times can thermally disorder the SL. The Ga over pressure appeared to preserve the structure since the PL was very similar before and after annealing. The As over pressure, in contrast, enhanced the disordering in the SL, and the peak was shifted to higher energy. It is important to consider the disordering that can occur during annealing and its effects on device performance.

3.7 CONSIDERATIONS RELATIVE TO DFB/DBR LASER FABRICATION

The structure examined in this work is to be incorporated in a distributed feedback type laser. The resolution of the selective ion beam implantation is an important factor in the development of such a device. The beam width coupled with the implant dose determines which grating order can be attained. Lower order gratings provide the strongest feedback, however, the required line widths are very narrow. A second order grating, for example, requires a line width of $\sim 1200\text{\AA}$. If the focused ion beam writing can be well controlled and the active region is not damaged, then a DFB laser would be the most efficient way to take advantage of the distributed feedback capability and to achieve the desirable lasing characteristics of a frequency-dependent feedback structure.

In a DFB laser, higher order gratings (fourth order, for example) can provide enough feedback to sustain laser operation, and the feedback is integrated with the gain medium. The disordered SL (AlGaAs alloy) must still be of optical quality so that the evanescent wave can interact with the grating without being absorbed. The alloy will have a wider band gap than the superlattice and the GaAs quantum well, and thus absorption should not be a dominant loss process. Losing carriers to nonradiative recombination at the ordered/disordered SL interfaces could increase the threshold power.

In contrast to a DFB laser, there is no potential damage to the active region in a DBR laser since only the end mirrors are corrugated. This will also allow for the tunneling of carriers from the SL to the QW without the losses due to the grating interfaces. With a higher order grating, however, the coupling is rather low and the extended mirror regions may have to be quite long in order to develop a standing wave in the cavity. There will also be some absorption in the unpumped mirror regions which will increase the threshold power.

Considering the optical properties of the multiple quantum well array, it is suitable for either DFB or DBR laser development. The limitations in the disordering and the preserving of the superlattice, the resolution of the selective ion beams, as well as the coupling capabilities of the grating will determine which configuration is the most beneficial.

4.0 MATERIALS EVALUATION OF MULTI QUANTUM WELL - SUPERLATTICE SAMPLES FABRICATED BY MOLECULAR BEAM EPITAXY

4.1 CROSS-SECTIONAL TRANSMISSION ELECTRON MICROSCOPY (X-TEM) FOR STRUCTURAL ANALYSIS

The superlattice (S/L) samples prepared for these experiments were fabricated at North Carolina State University (Electrical Engineering Department) using the Varian MBE system described in Section 3.1.1. The structure of the samples was based on having an active GaAs quantum well (QW) approximately 300Å thick positioned above an AlGaAs buffer layer with a superlattice stack above the QW and a top 500Å capping layer of AlGaAs above the S/L. The thicknesses of the superlattice wells and barriers were typically in the range 35 to 50Å. This design was chosen for its relevance to the laser device that is being considered for development. Figure 21 is a cross-sectional TEM micrograph of such a sample showing the relative position of the various component layers.

Sample preparation for cross-sectional TEM analysis, as presented in Figure 22, is a well developed capability at UES. A full description of the process involved in preparing and evaluating such samples is given by A.K. Rai et al. [28] in the Journal of Electron Microscopy Technique (1987).

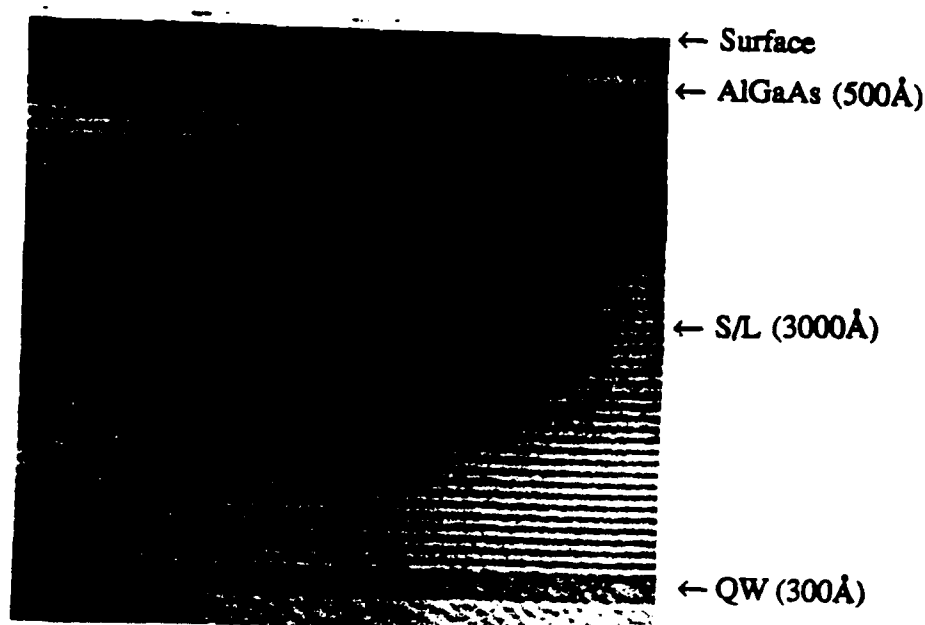


Figure 21. X-TEM Bright Field Micrograph of a Multi-Quantum Well/Superlattice (MQW/SL) Used in These Experiments.

4.2 SPUTTER AUGER COMPOSITIONAL PROFILING

Auger depth profiling of the QW/SL samples was performed at the University of Dayton Research Institute using both the 68 eV and 1396 eV aluminum lines. The spatial variation of aluminum in these samples is a critical parameter for determining the level of compositional mixing and, therefore, the local refractive index. In some cases the Ga and As concentrations were also monitored to confirm the overall structural composition of the material. Figure 23 shows the general compositional variation across the entire thickness of an unimplanted QW/SL sample from the surface all the way through the capping layer, superlattice, lower quantum well and finally the AlGaAs buffer layer. This is a low depth resolution profile showing a systematic variation in the gallium, arsenic, and aluminum concentrations throughout the depth of the sample. These results compare favorably to the structural pattern seen in the X-TEM micrograph of Figure 21.

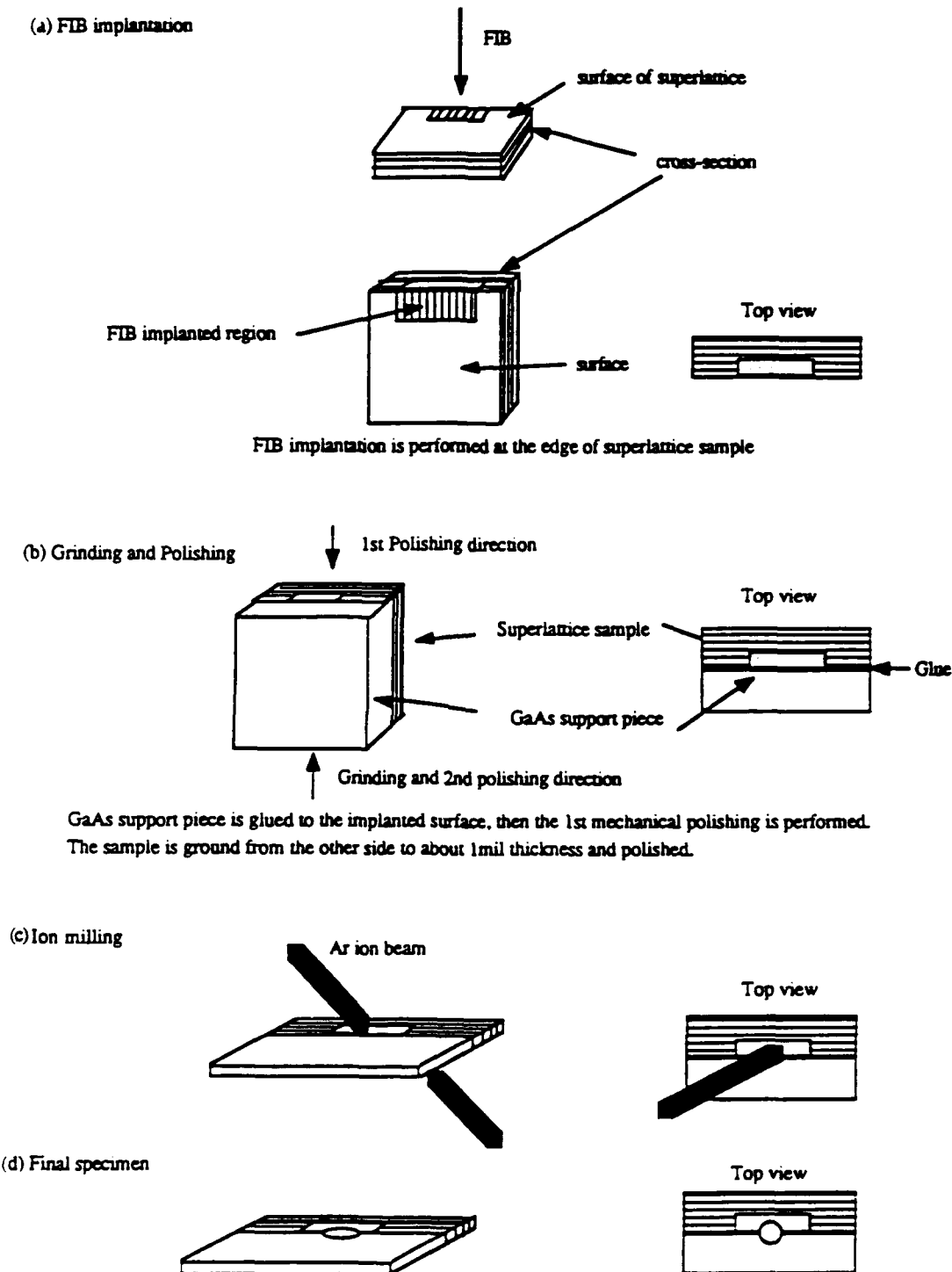


Figure 22. Schematic of TEM Sample Preparation.

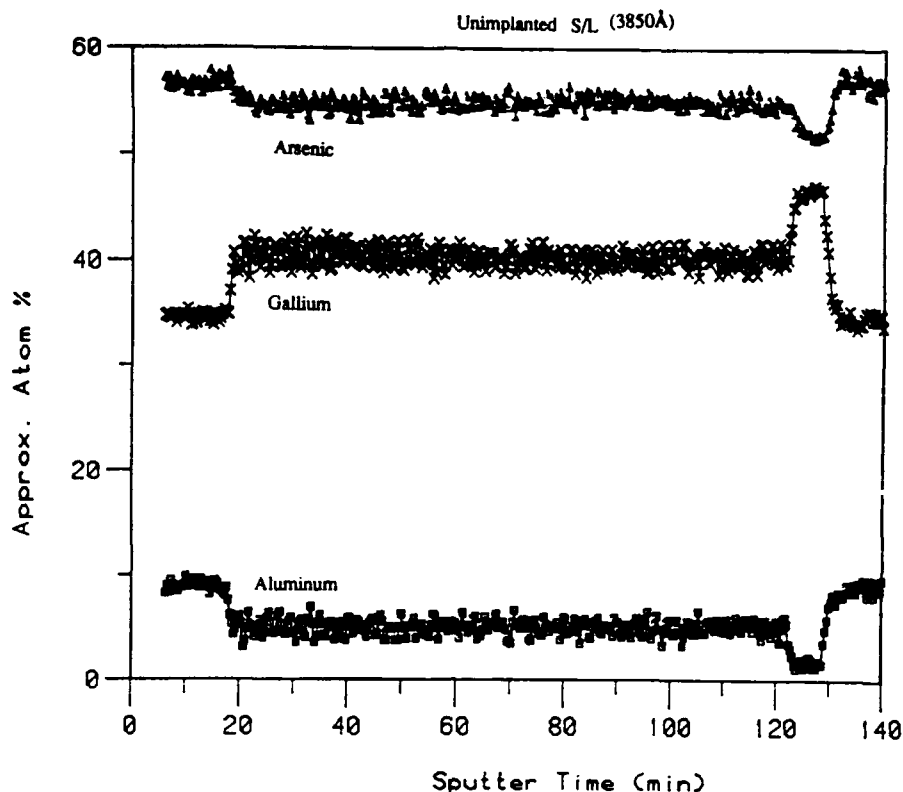


Figure 23. Low Resolution Auger Compositional Depth Profile of Entire Thickness of QW/SL Sample.

A higher resolution profile is available by sputtering at a slower rate and monitoring the 68 eV Al line. Detailed information on the spatial variation of aluminum is obtainable by this method. Figure 24 shows such a profile for the first half of QW/SL material which had been implanted with a $5 \times 10^{13} \text{ cm}^{-2}$ fluence of Ga^+ ions at an energy of 890 keV. Clearly visible in this compositional profile is the top most capping layer which is sputtered through in the first 20 minutes. The noise level which is superimposed on the Al signal is defined by the fluctuation in the Al signal across this initial capping layer. The aluminum concentration in the superlattice region is observable after the initial 20 minute period and is discernable as a systematic set of peaks as the Al signal from the sputter profiling sequentially changes as the beam profiles through the GaAs and then the AlGaAs. Each layer in the superlattice region is approximately 50Å. It is seen in Figure 24 that the discreteness of the superlattice is clearly discernable and very well defined relative to the aluminum background noise. This shows that the implant parameters used in this sample did not induce any significant degree of mixing.

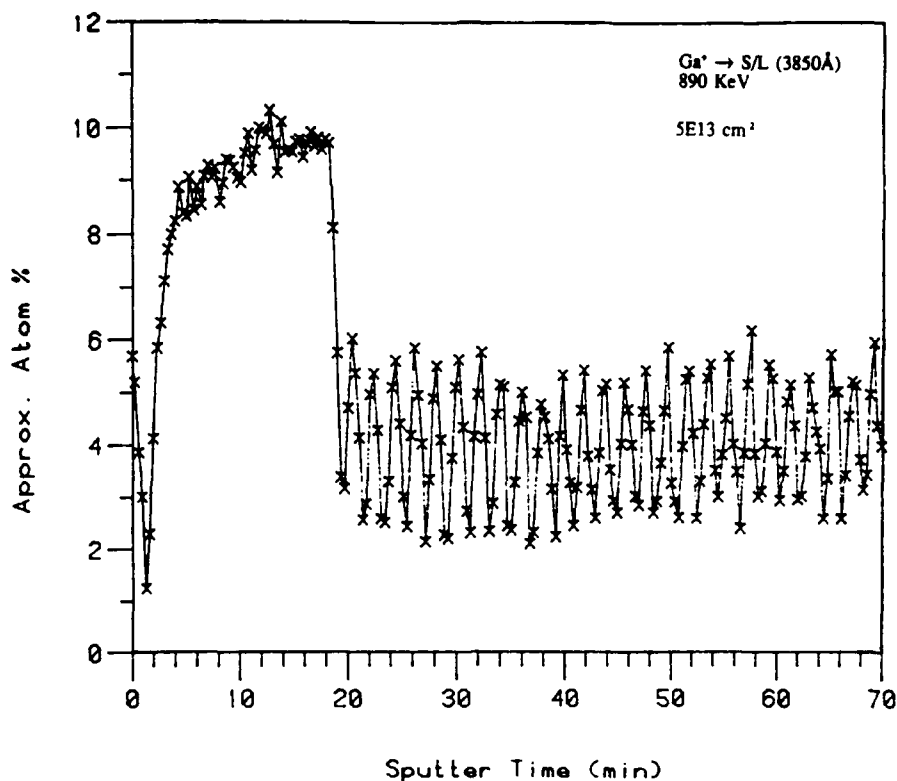


Figure 24. High Resolution Auger Compositional Depth Profile of First Half of QW/SL Sample.

When the superlattice becomes compositionally mixed this systematic variation in Al will disappear and collapse into a band of noise across the superlattice region. These effects will be discussed more fully in following sections where the results of superlattice mixing are presented.

5.0 ION MIXING IN SUPERLATTICE SYSTEMS

As described in Figure 7 of Section 3.1, ion implantation and associated ion mixing are to be used and tested as a method for fabricating optical laser gratings. A two dimensional diagram is presented in Figure 7 showing the relationship of the ion implanted regions to the unimplanted superlattice zones. In Figure 25 below we present a three dimensional drawing of the MQW/SL structure that is used in these experiments with a depiction of the ion implanted grating lines that are to be embedded in the superlattice region of the structure. The structure as shown in Figure 25 represents the type of sample that was used for the photo-pumped laser measurements presented throughout Section 3. The remainder of this report discusses work that was done to define, control, and test the fabrication of the grating line structures using ion implantation and ion beam mixing.

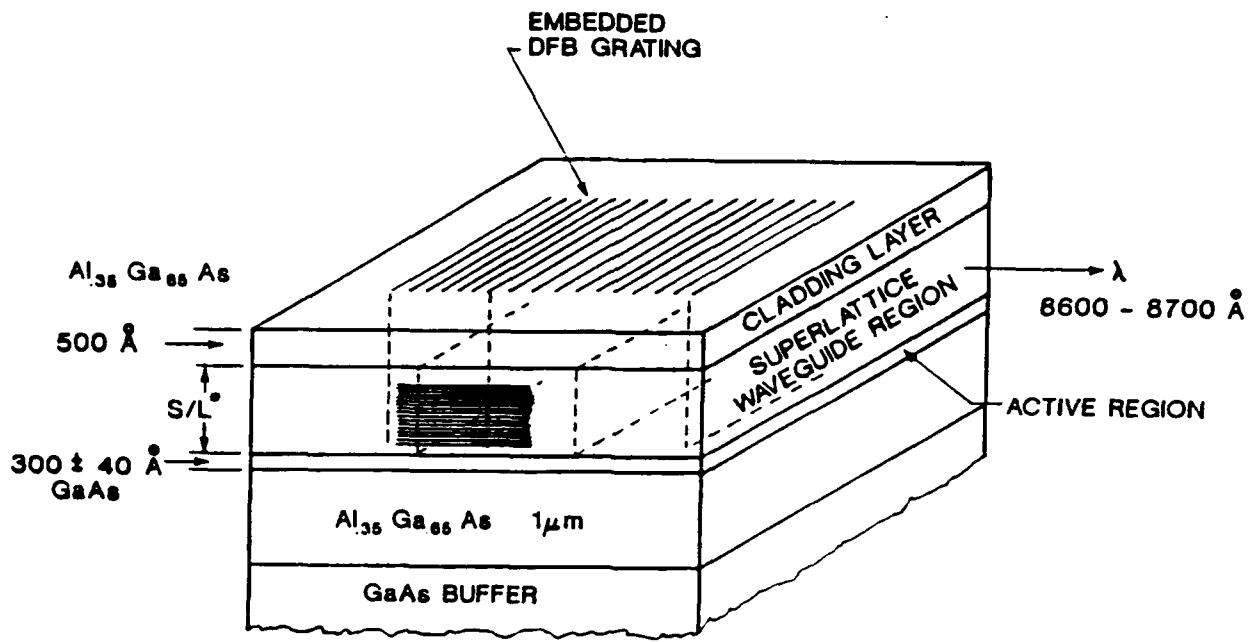


Figure 25. Initial Design and Structure of MQW/SL - DFB Laser.

As shown in Figure 26 below, two approaches to this process technique have been tested. The block diagram shows the optional approaches relative to the fabrication techniques available. The grating lines formed by ion mixing can then be fabricated using either Ga ions at energies up to 900 keV or Si ions at 250 keV nominal energies. These two ions were chosen for specific reasons. The first is that Ga ions at approximately 900 keV will penetrate the entire SL structure and produce an aluminum redistribution by cascade mixing with little or no contribution from chemical effects. Conversely, Si ions at 250 keV will produce very little collision mixing, due to it being a relatively light ion, but will contribute a strong chemical effect on aluminum redistribution under subsequent heat treatment and annealing.

Following these tests and pending their outcomes, the ion beams will be used to fabricate a grating pattern. Rather than try to use fine line ($1/4 \mu\text{m}$) masking techniques, it has been decided that the use of a focused ion beam (FIB) system represents a more viable approach for this purpose.

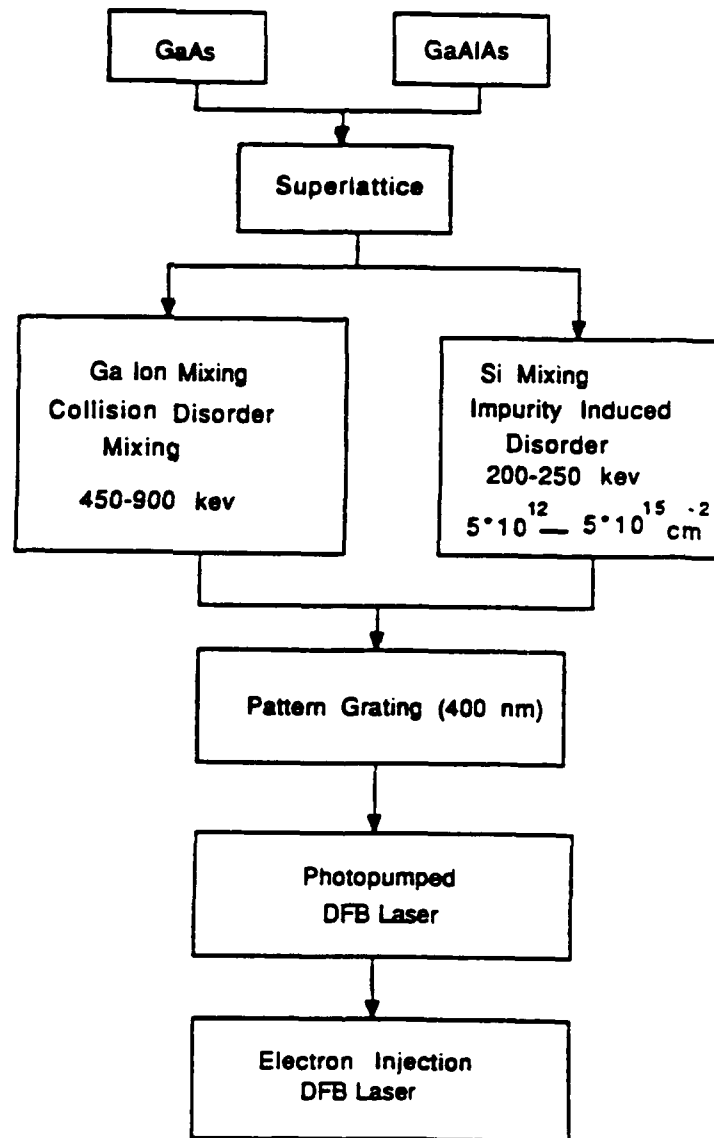


Figure 26. Block Diagram Showing Approaches to Fabricating Ion Mixed Grating Structure for DFB Laser Application.

5.1 SUPERLATTICE DISORDERING FROM CASCADE MIXING UNDER Ga ION IMPLANTATION

It is anticipated that Ga ions (masses 69 thru 71) will be sufficiently heavy that moderate doses will result in very little chemical change, but very significant physical change through heavy ion collision cascade radiation displacement damage. In order to determine the fluence levels necessary to accomplish these effects we performed a series of experiments on damage fluence relationships for Ga ions in GaAs and also in AlGaAs. The energies chosen for these tests were appropriate to Ga penetrating through the geometry of the chosen superlattice structure. As will be seen below, the damage-fluence behavior of GaAs is found to be radically different than that for AlGaAs where the Al content is nominally 30 at.%.

The vertical dimensions of our proposed laser device will dictate the energies required for penetration through the SL structure in order to effect the necessary mixing. Ion implantation produces a depth distribution of damage with a modified Gaussian like shape. Our initial objective was to place the peak of this damage distribution at the center of the superlattice structure. Figures 41 through 43 in Appendix I show the results of range and damage calculations carried out using our TRIM 87 and 88 Monte Carlo code along with other relevant data on collision cascades. The target used in these calculations is $\text{Al}_{0.3}\text{Ga}_{0.7}\text{As}$. Information on mean range and straggling were extracted from such data and used to establish appropriate ranges of ion energies to be tested.

We have studied the response of GaAs and $\text{Al}_{0.35}\text{Ga}_{0.65}\text{As}$ individually and as a superlattice, to ion implantation (cascade) damage at room temperature. Gallium ions at 890 and 960 keV were used in the fluence range of 10^{13} to 10^{15} ions/cm². These energies were chosen to correspond to implant damage and mixing in 3000Å and 4000Å superlattice stacks where the mean projected ranges (R_p) are approximately 4000 and 4300Å, respectively. Implant fluence levels were chosen to produce damage that ranged from lightly dispersed (10^{13} cm⁻²) to very dense and ultimately to saturated damage (10^{15} cm⁻²). The dynamic progression of the system to an amorphous phase in the high damage regime was of particular interest.

We observed in these superlattices that the GaAs layers accumulate damage more rapidly than the AlGaAs layers, a result consistent with literature reports of others [29]. There is a need, therefore, to clarify the damage production and retention processes occurring in these systems and the extent to which it is a property of the superlattice or an intrinsic property of the individual materials that make up the superlattice. We demonstrate below that the preferential build up of damage in GaAs is an intrinsic property of the GaAs compared to $\text{Al}_{0.35}\text{Ga}_{0.65}\text{As}$, there being a distinct and radical difference between the room temperature annealing characteristics of these two materials and, therefore, a difference in the amount and the nature of the heavy ion collision damage retained by each.

The intermixing of superlattices as a controllable and spatially selectable process has received considerable interest in the literature [30]. This has been an outgrowth of the discovery that chemical intermixing of superlattices can be achieved by the in-diffusion of certain chemical species [31,32]. In the case of Al in GaAs/AlGaAs, it has been found that Zn [31] or Si [32] act as disordering species. The chemical disordering achieved in this way has also been produced by ion-implanting these same diffusional species and then subjecting the system to a thermal annealing cycle in order to re-distribute them [33]. In so doing, a chemical intermixing of the superlattice occurs. Implantation damage has been found to play some role in the compositional disordering during these annealing cycles [34].

In general, the superlattices of interest will have periodicities of $<100\text{\AA}$. In such cases, it is reasonable to expect that cascade intermixing of the AlGaAs with the GaAs layers can be achieved. This should occur as a result of dynamic collision cascade events where net transport of Al occurs thru dense sub-cascade atomic intermixing which is known to occur across dimensions of $<100\text{\AA}$. This is especially true in highly miscible systems such as GaAs/AlGaAs.

Samples were analyzed by various techniques: RBS channeling (RBS-C), cross-sectional transmission electron microscopy (X-TEM), and sputter Auger analysis.

5.1.1 Ga Implantation in GaAs - Calibration of Cascade Damage Production

Prior to evaluating compositional mixing from the collision cascade process, it is instructive and sensible to determine the extent of damage production in binary GaAs and the fluence levels needed, at these energies, to produce multiple DPA (displacements per atom) events that will, in addition to mixing, ultimately lead to amorphization of the crystalline material. The fluence levels normally used for ion beam mixing of such layers (10^{15} to 10^{16} cm^{-2}) should produce amorphous conditions in GaAs under room temperature bombardment. Figure 27 is an RBS channeling spectrum for bulk GaAs material which was subjected to 960 keV Ga^+ bombardment to fluence levels of 4×10^{13} , 7×10^{13} , and 1×10^{14} cm^{-2} . It is clear from these results that a fluence level of approximately 2×10^{14} cm^{-2} will result in a GaAs channeling spectrum with a yield equivalent to the random yield representing an amorphous layer with maximum damage and mixing in the range of 2000 to 4000 Å.

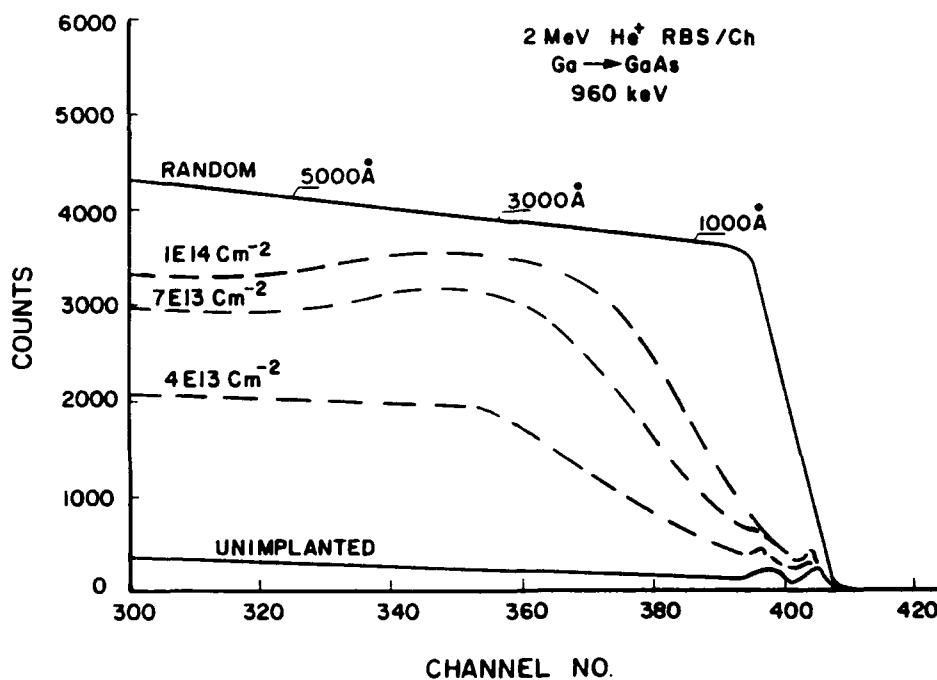


Figure 27. RBS-Channeling Spectra. 960 keV Ga Implanted GaAs.

5.1.2 Ga Implantation in AlGaAs/GaAs S/L and Bulk AlGaAs

Comparison of the channeling results for GaAs (Figure 27) with that of our S/L (Figure 28) shows that in the S/L a fluence of $3.88 \times 10^{14} \text{ cm}^{-2}$ results in less than 50% total damage. Further comparison of Figure 28 with the S/L X-TEM results of Figure 29 shows that the GaAs quantum well sustains more damage than the AlGaAs portion of the S/L and that the AlGaAs capping layer has retained very little observable damage. This is further supported by the near surface crystal string channeling oscillations in the AlGaAs capping layer.

Additionally, examination of the X-TEM micrograph of Figure 29 reveals heavy black spot damage clusters in the GaAs quantum well and the GaAs portions of the S/L but very little clustered damage in the AlGaAs capping layer and the AlGaAs portions of the S/L. In order to further understand these effects, a bulk specimen of AlGaAs was implanted with Ga at 890 keV with fluences ranging from $1 \times 10^{13} \text{ cm}^{-2}$ to $1 \times 10^{16} \text{ cm}^{-2}$. Figure 30 shows the RBS channeling spectra obtained from that sample. It is clear from these results that the AlGaAs is building its damage level at a much lower rate than the GaAs. The spectra in Figure 30 have the characteristic appearance of dechanneling spectra. These are typical results normally seen for heavy ion damage in ionic crystals where amorphous damage zones are not retained, but in their place are observed small clusters of defects such as Frank loops embedded between the crystal planes of the host lattice. This result argues in favor of a very rapid room temperature annealing process that allows the material to retain its crystallinity with the displacement damage accommodated in clustered interstitial or vacancy loops. This response to heavy ion damage is known to be very temperature dependent for ionic crystals or for compound semiconductor material that exhibits a high degree of ionic bonding. In fact, it is usually possible to achieve some degree of amorphization by reducing the bombarding temperature to the liquid nitrogen temperature range. The binary compound AlAs has been shown to become amorphous under ion bombardment at 77K [35]. However, for room temperature bombardment, it is clear from Figure 30 (as well as from TEM analysis) that the crystallinity of the AlGaAs material is retained. Notwithstanding this effect, it is also clear that under heavy ion bombardment, there

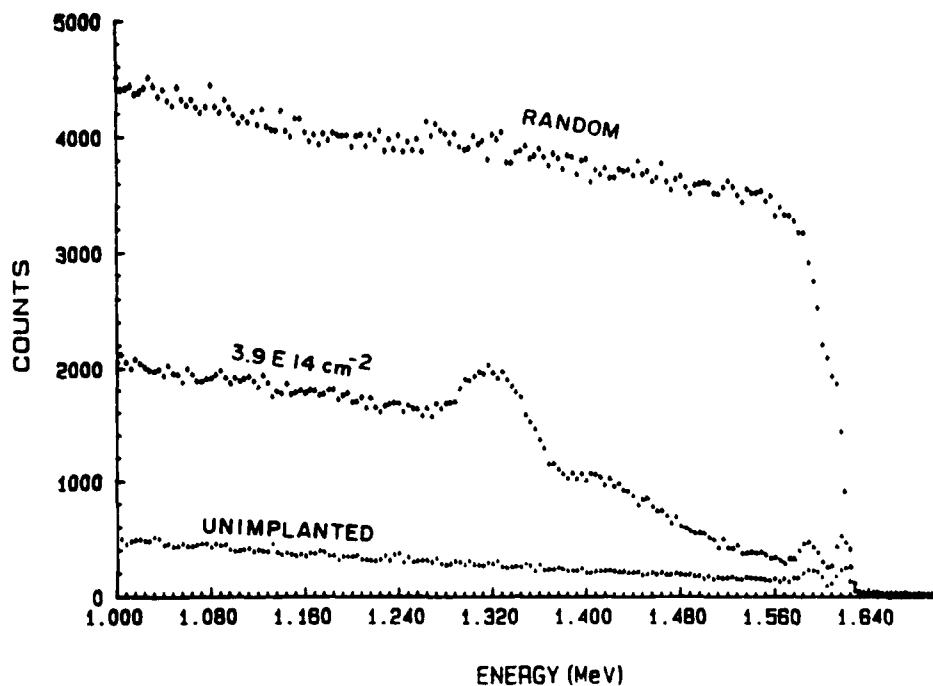


Figure 28. RBS-Channeling Spectra. 960 keV Ga Implanted MQW/SL of Figure 21.

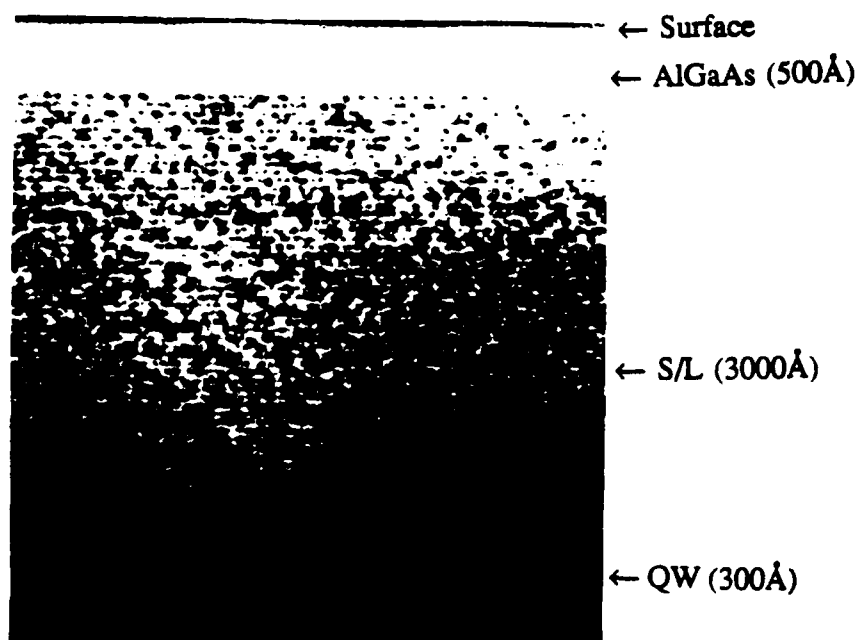


Figure 29. X-TEM MQW/SL of Figure 21 After Implant. 960 keV, $1 \times 10^{14} \text{ cm}^{-2}$ Ga.

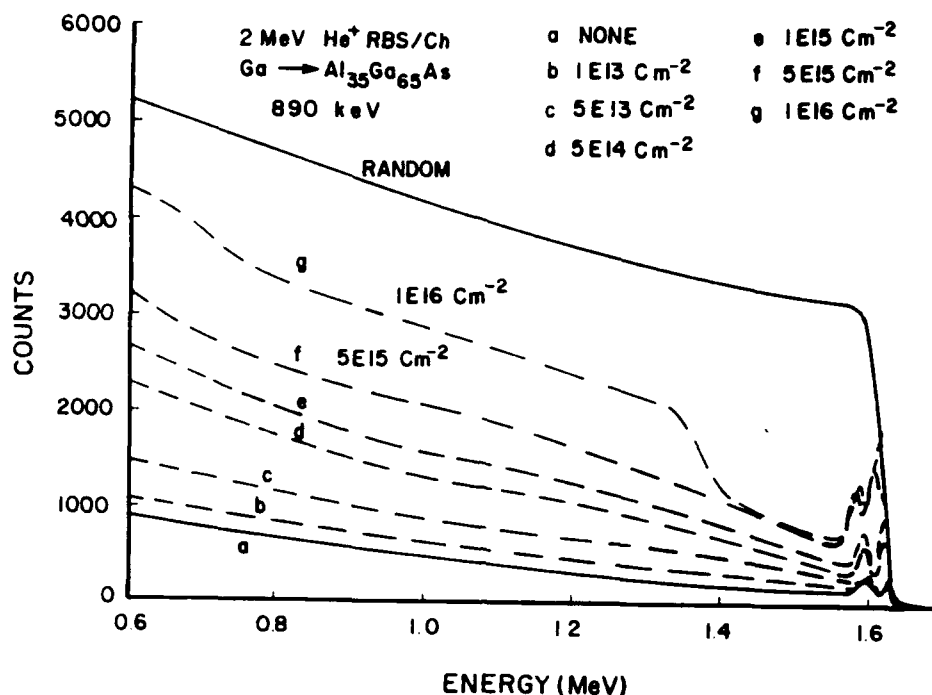


Figure 30. RBS Channeling Spectra. 890 keV Ga Implanted AlGaAs

will be a large DPA rate in effect and the aluminum atoms in the AlGaAs will in fact be displaced many times and transported distances on the order of 25, 50 or 100Å by the dynamic mixing effects of the collision subcascades. In view of this, continued bombardment of the S/L should result in eventual transport of aluminum out of the AlGaAs and into the GaAs. Since the GaAs will become amorphous prior to extensive mixing of the Al into it, a continued amorphous condition will be sustained during and after Al intermixing into the original GaAs material. However, as the Al is depleted from the AlGaAs, the high degree of ionic bonding will be converted to the more co-valent bonding of the GaAs type material and at some minimum critical concentration of Al, it too becomes amorphous under RT bombardment.

In order to confirm that the S/L could be driven into the amorphous state, we continued with bombardment of the S/L up to $5 \times 10^{14} \text{ cm}^{-2}$ Ga ions. Figure 31 shows the RBS channeling spectra for this case and confirms the above argument that a sufficient re-distribution of Al

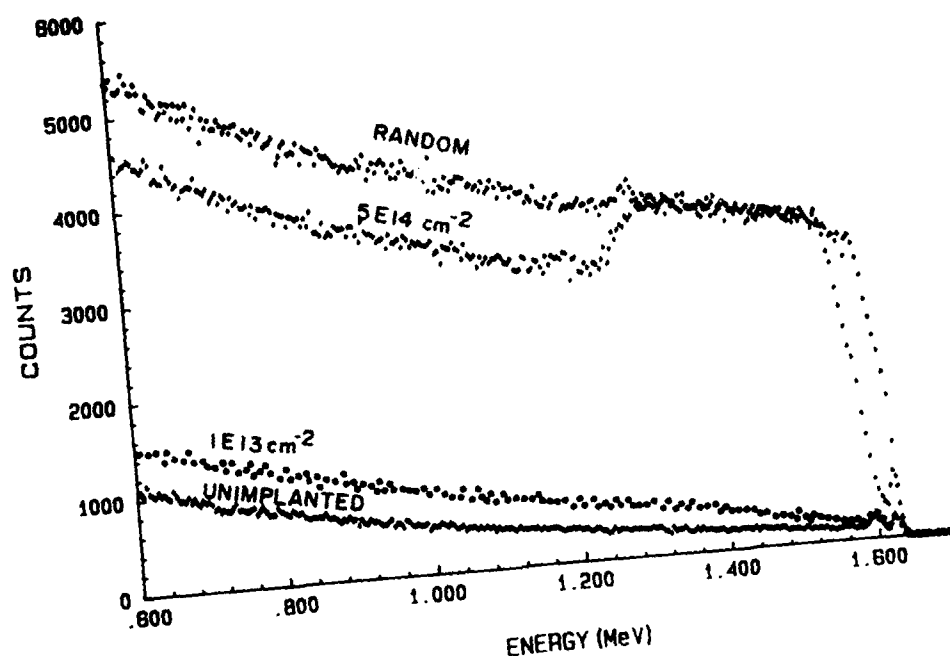


Figure 31. RBS-Channeling Spectra. 890 keV Ga Implanted MQW/SL of Figure 21.

occurs across the 35 to 50Å superlattice layer to achieve a uniform and compositionally average aluminum concentration necessary for amorphization.

Confirmation of the mixing achieved by Ga implantation of the superlattice is provided by Auger compositional depth profiling. Figure 32 shows the 64 eV Al Auger signal before implantation and after implantation with 890 keV Ga⁺ ion fluences of 5×10^{13} , 1×10^{14} and $5 \times 10^{14} \text{ cm}^{-2}$. The initial well-defined periodicity of the Al signal shows an increasing degradation with ion fluence until a state of complete homogeneity is achieved after implanting with a fluence of $5 \times 10^{14} \text{ cm}^{-2}$. The complete mixing achieved by the highest dose corresponds to the condition of amorphization shown in Figure 31. Thus, achieving amorphization in this system is a sufficient condition for mixing.

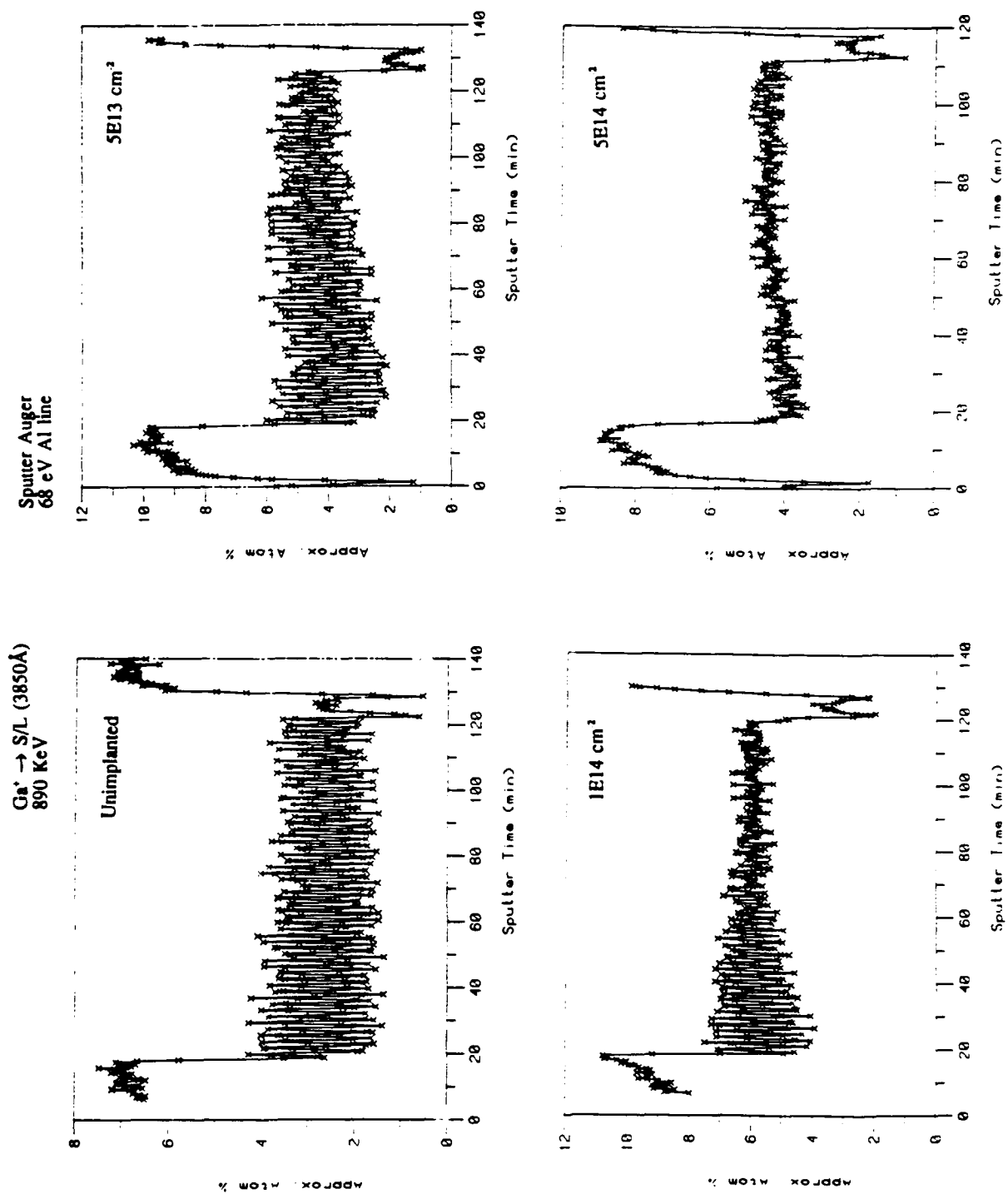


Figure 32. Auger Al Composition Depth Profiles of Ga⁺ Implanted QW/SL Samples.

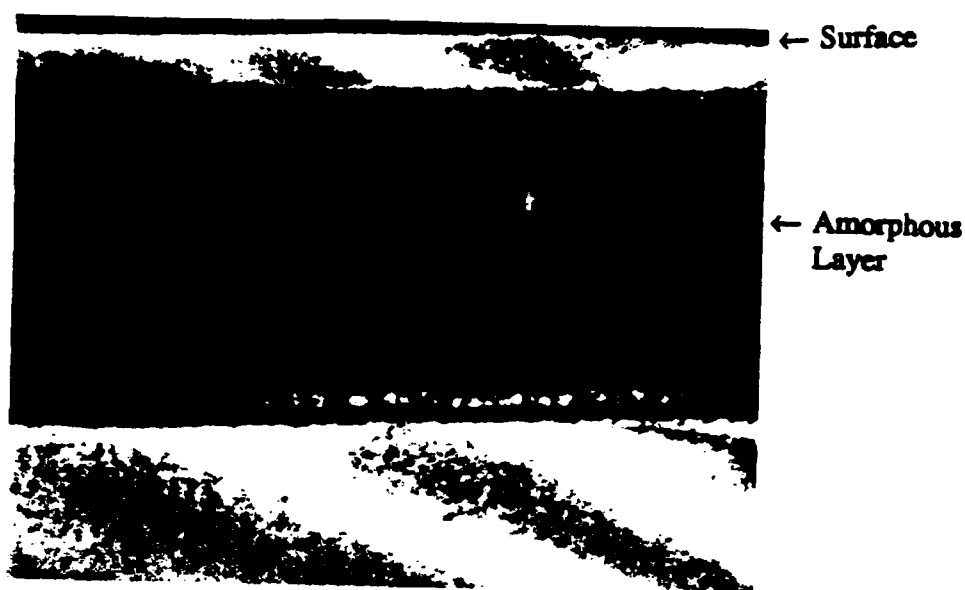
5.1.3 Annealing of Ga Implanted S/L Material

In order to utilize ion beam mixing for DFB or DBR laser grating fabrication it is necessary to reduce the level of crystal damage so that absorption losses are minimized. Consequently, TEM cross section analysis was carried out on AlGaAs/GaAs superlattice samples that had been implanted with 890 keV Ga^+ ions and had been annealed at 850°C for 1 min. The fluences used in this investigation ranged from $1 \times 10^{14} \text{ cm}^{-2}$ to $1 \times 10^{16} \text{ cm}^{-2}$.

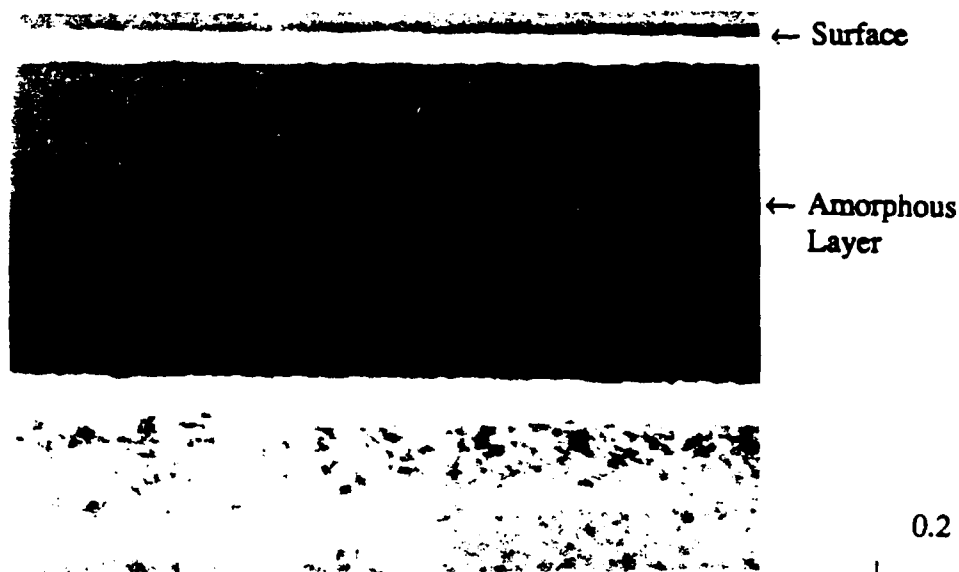
Figure 33 shows dark field TEM micrographs of superlattice material that had been implanted with 5×10^{14} and $1 \times 10^{16} \text{ cm}^{-2}$ fluences but was not annealed. In both cases, an extensive buried amorphous layer, identified by the dark band, overlaps the original location of the superlattice. It is assumed that the 3850Å superlattice is completely mixed after these implantation fluences. On either side of the buried amorphous layers the material retains its crystalline character, but contains substantial densities of defects.

Figure 34 shows dark field TEM micrographs of superlattice material that had been implanted with 1×10^{15} and $1 \times 10^{16} \text{ cm}^{-2}$ fluences of 890 keV Ga^+ ions after annealing. For both fluences, the material is crystalline but contains a large density of defects. The active GaAs quantum well layer is now visible although there is no trace of the short period superlattice. A large density of dislocation tangles are located in the layer above the quantum well which originally consisted of the superlattice. Presumably, this band of defects is located at the point where the solid phase regrowth boundaries met during the anneal. For both fluences a considerable density of dislocation loops remains in the AlGaAs cladding layer below the quantum well.

Bright field TEM cross section micrographs of Ga^+ implanted and annealed superlattice material are shown in Figure 35 for fluences 1×10^{14} , 1×10^{15} and $1 \times 10^{16} \text{ cm}^{-2}$. Residual defects are visible in all cases. The large density of dislocation tangles in the layer above the GaAs quantum well for the 1×10^{15} and $1 \times 10^{16} \text{ cm}^{-2}$ Ga^+ fluence samples are consistent with Figure 34. Since no superlattice structure is observed for any of the Ga^+ fluences, all the implant and anneal schedules have achieved the desired mixing effect. However, from the point of view of requiring a low defect density in the crystalline material, only the $1 \times 10^{14} \text{ cm}^{-2}$ fluence appears to be suitable for the adopted anneal conditions.

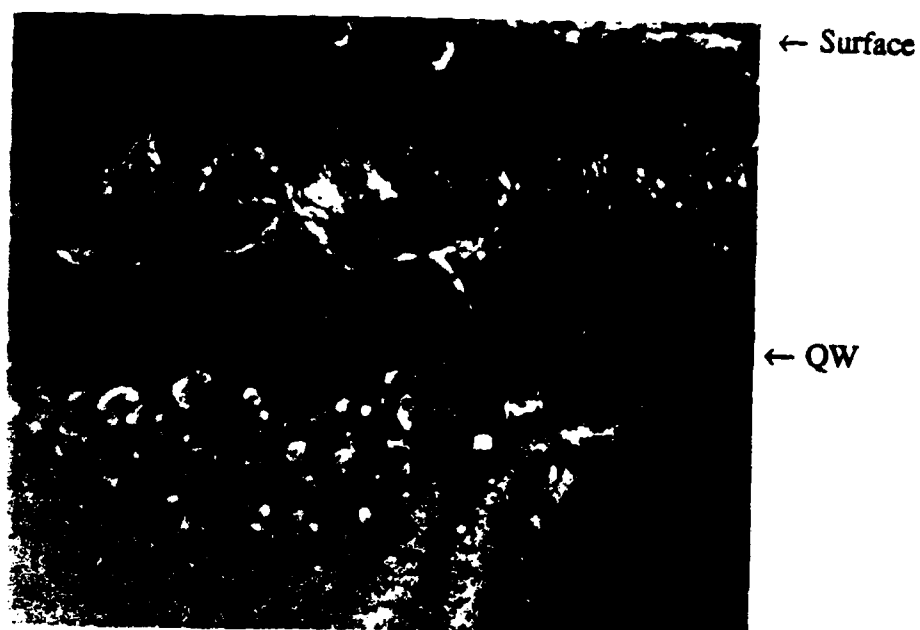


(a)

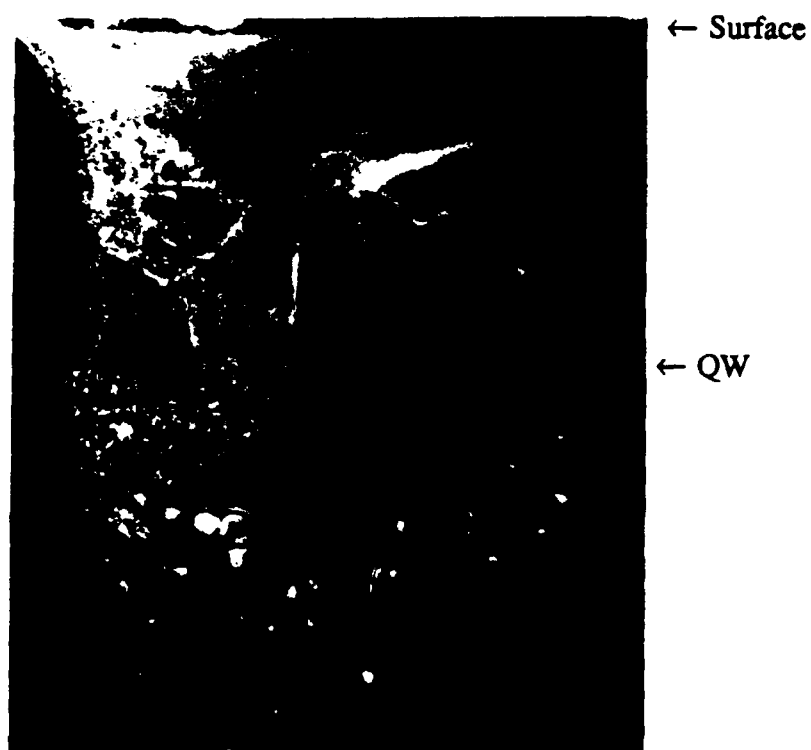


(b)

Figure 33. Dark Field TEM Cross Section Micrographs of QW/SL Material after Implantation with (a) 5×10^{14} and (b) $1 \times 10^{16} \text{ cm}^{-2}$ Fluences of 890 keV Ga^+ Ions.



(a)



(b)

Figure 34. Dark Field TEM Cross Section Micrographs of QW/SL Material after Implantation with (a) 1×10^{15} and (b) 1×10^{16} cm^{-2} Fluences of 890 keV Ga^+ Ions and Annealing at 850°C for 1 min.

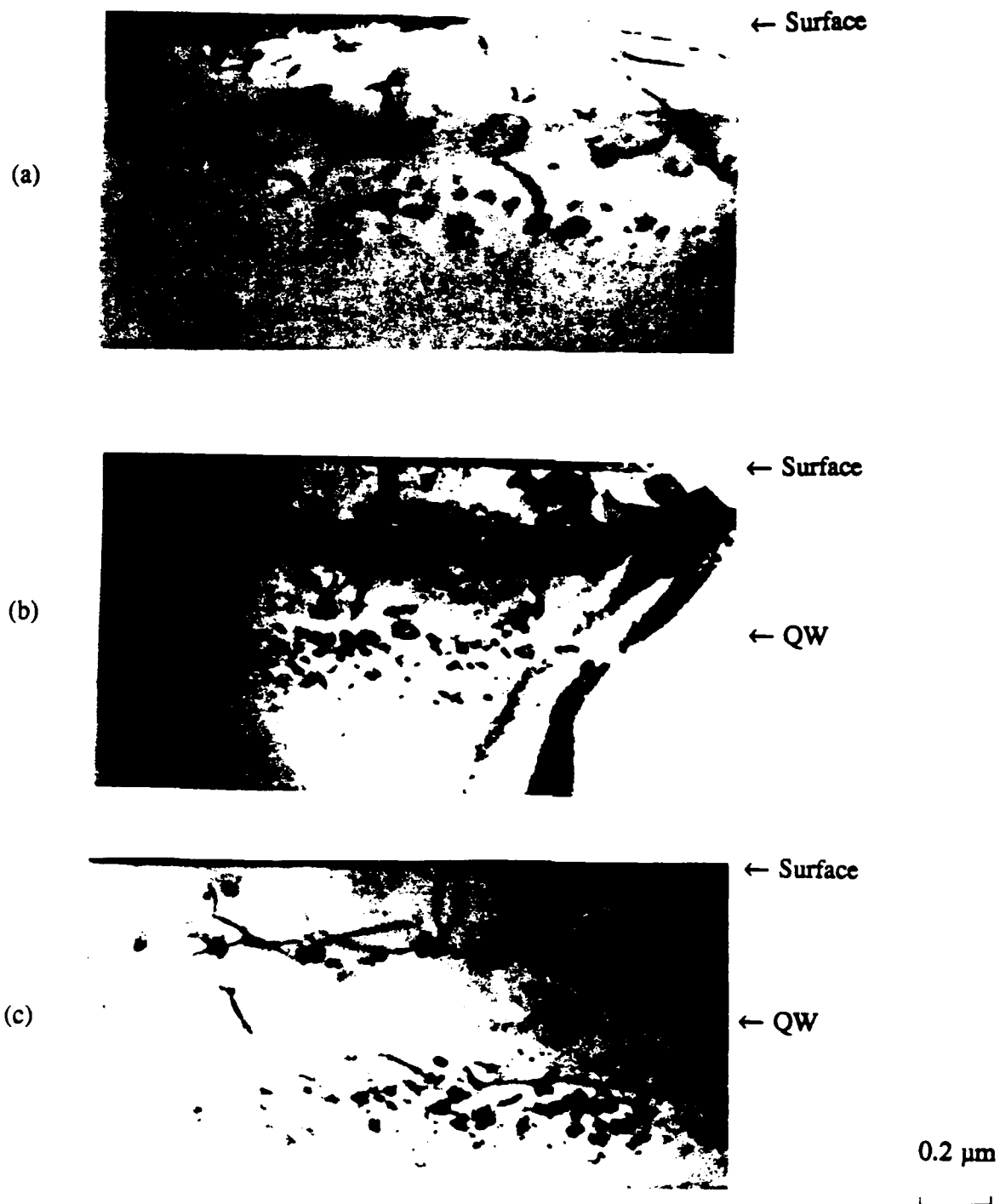


Figure 35. Bright Field TEM Cross Section Micrographs of QW/SL Material after Implantation with (a) 1×10^{14} , (b) 1×10^{15} , and (c) $1 \times 10^{16} \text{ cm}^{-2}$ Fluences of 890 keV Ga^+ Ions and Annealing at 850°C for 1 min.

5.2 SUPERLATTICE DISORDERING UNDER Si ION IMPLANTATION

Broad beam Si^+ implantation of AlGaAs-GaAs superlattice samples was carried out to investigate the chemical disordering effect and defect production. The energy of broad Si^+ beam implantation was 250 keV. The doses used were $5 \times 10^{13} \text{ cm}^{-2}$, $1 \times 10^{14} \text{ cm}^{-2}$, $1 \times 10^{15} \text{ cm}^{-2}$, $5 \times 10^{15} \text{ cm}^{-2}$, and $1 \times 10^{16} \text{ cm}^{-2}$. After implantation, rapid thermal annealing at 1050°C for 10 sec was carried out in a graphite pill box. During the anneal, the implanted samples were sandwiched between GaAs wafers to minimize surface dissociation.

Secondary ion mass spectrometry (SIMS) was used to measure the implanted impurity depth profiles. Cross section photographs of the samples were taken with a transmission electron microscope (TEM).

The SIMS results are shown in Figures 36-38. Although the SIMS measurements were unable to resolve the periodicity of the aluminum concentration in the superlattice (0.15 to 0.42 μm), they were able to detect the 33 nm wide GaAs quantum well immediately beyond the superlattice. No significant variation in the aluminum profile is seen for Si doses 1×10^{15} to $1 \times 10^{16} \text{ cm}^{-2}$, suggesting that for these implant and anneal conditions no significant mixing of the quantum well takes place. Since the implanted silicon distribution has a measured projected range of $\sim 310 \text{ nm}$, the peak of the damage distribution is expected to be located substantially closer to the surface and, therefore, the quantum well should be relatively damage-free. This phenomena is supported by the TEM cross section photographs shown in Figures 39 and 40.

In Figure 39(a) (dose = $5 \times 10^{13} \text{ cm}^{-2}$), the superlattice structure is quite evident and disordering is insignificant. In Figure 39(b) (dose = $5 \times 10^{14} \text{ cm}^{-2}$), the superlattice has become partially mixed. Notice that in this case, the defects exist only in the superlattice region and the quantum well is not damaged. A similar degree of mixing and location of defects is seen in Figure 40(a) for a Si^+ dose of $1 \times 10^{15} \text{ cm}^{-2}$. However, for a $1 \times 10^{16} \text{ cm}^{-2}$ dose, shown in Figure 40(b), the superlattice is completely mixed and dislocation loops extend beyond the quantum well. In this case, it appears that the quantum well is partially mixed since the interfaces are not as clearly defined as for the lower dose implanted material.

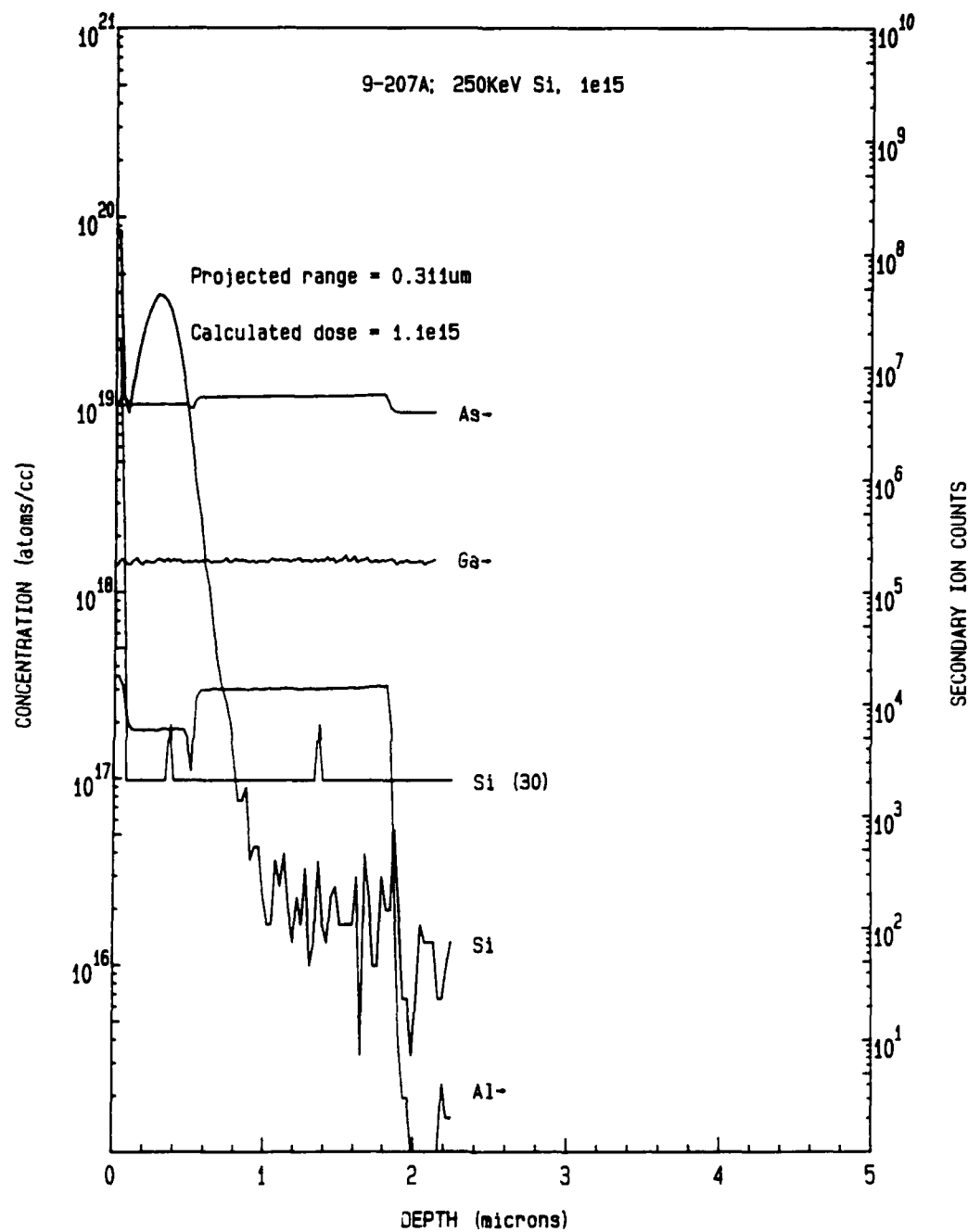


Figure 36. SIMS Impurity Profile of Broad Beam Implanted Quantum Well Laser Material (Dose = $1 \times 10^{15} \text{ cm}^{-2}$).

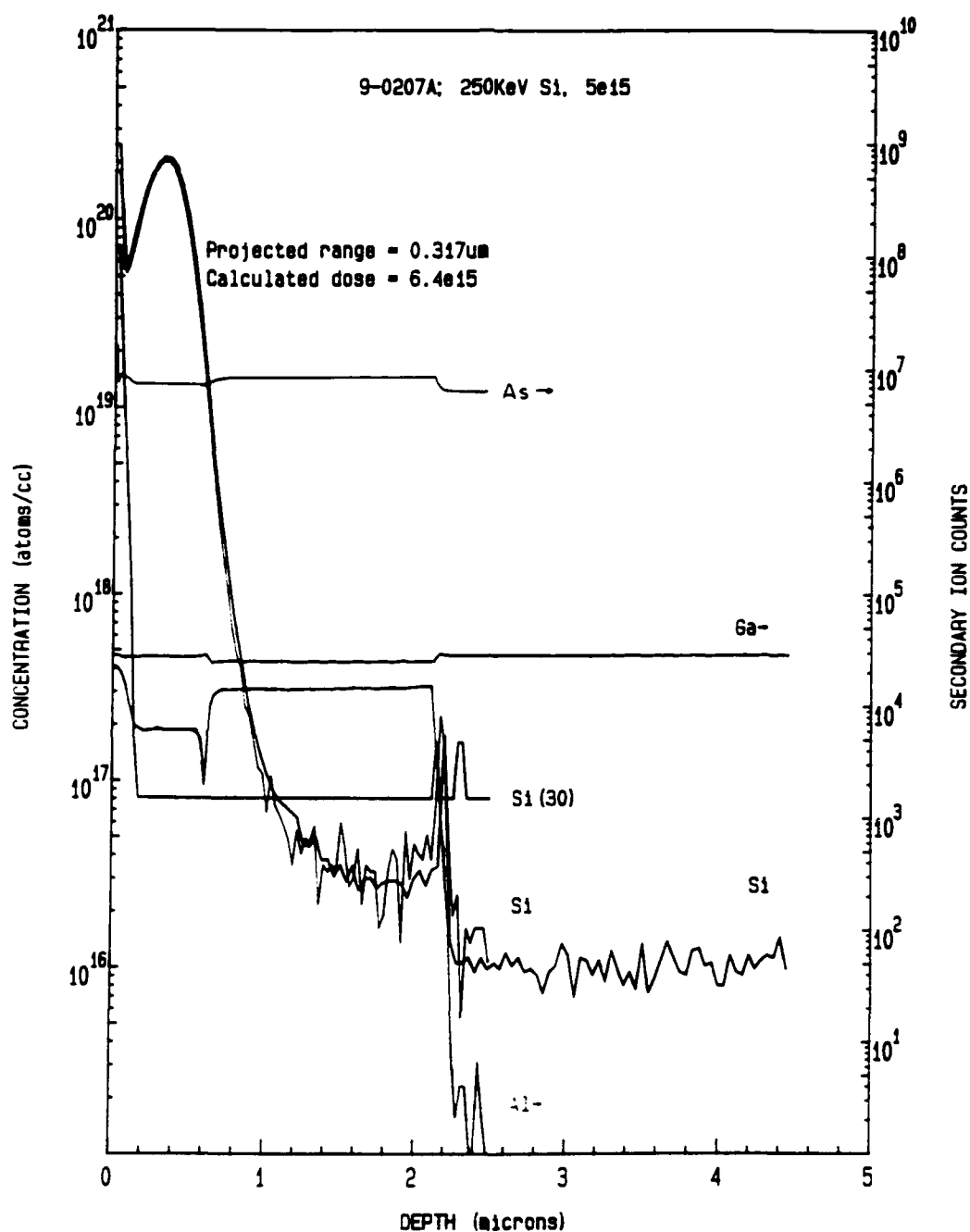


Figure 37. SIMS Impurity Profile of Broad Beam Implanted Quantum Well Laser Material (Dose = $5 \times 10^{15} \text{ cm}^{-2}$).

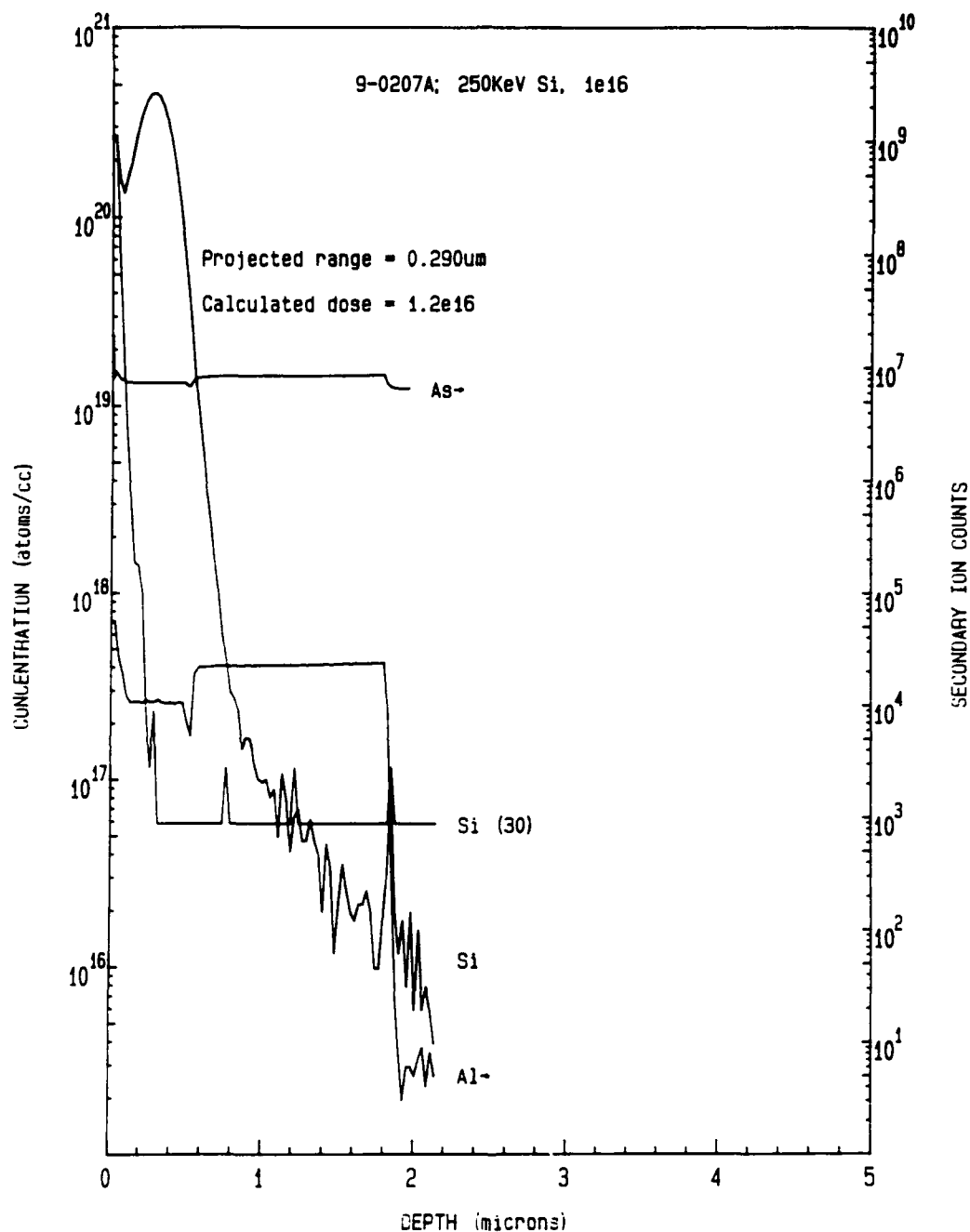
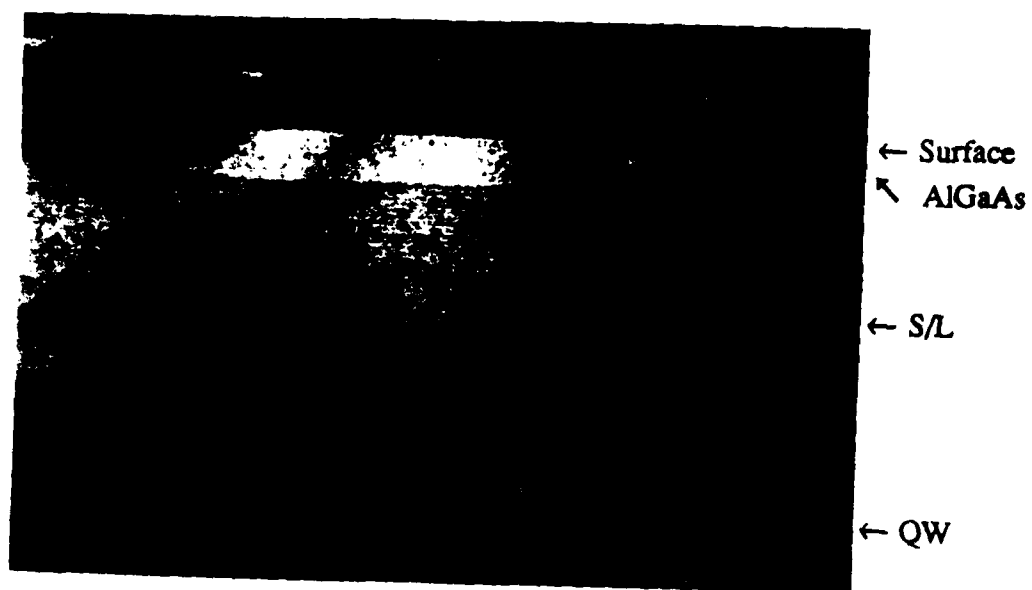


Figure 38. SIMS Impurity Profile of Broad Beam Implanted Quantum Well Laser Material (Dose = 1×10^{16} cm⁻²).



(a)



(b)

Figure 39. TEM Cross Sections of Laser Material Implanted with (a) $5 \times 10^{13} \text{ cm}^{-2}$, (b) $5 \times 10^{14} \text{ cm}^{-2}$ Doses of 250 keV Si^+ Ions and Annealed at 1050°C for 10 seconds.



(a)



(b)

Figure 40. TEM Cross Sections of Laser Material Implanted with (a) $1 \times 10^{15} \text{ cm}^{-2}$, (b) $1 \times 10^{16} \text{ cm}^{-2}$ Doses of 250 keV Si^+ Ions and Annealed at 1050°C for 10 seconds.

Based on SIMS profiles, the projected range of Si^+ into the superlattice material is about 310 nm, which is greater than the calculated Si^+ range in GaAs (250 nm from TRIM simulation). The reason for this effect is that the density of the superlattice is smaller than that of GaAs. Therefore, Si ions go deeper in the superlattice.

REFERENCES

1. G.P. Agrawal and N.K. Dutta, Long Wavelength Semiconductor Lasers (Van Nostrand Reinhold Company, New York, 1986).
2. Y. Nakano and K. Tada, Appl. Phys. Lett. 49, 1145 (1986).
3. K. Kojima, S. Noda, S. Tai, K. Kyuma, K. Hamanaki, and T. Nakayama, Appl. Phys. Lett. 49, 366 (1986).
4. S. Takigawa, M. Kume, K. Hamada, K. Tateoka, H. Naitoh, N. Yoshikawa, A. Yamamoto, H. Shimizu, and K. Itoh, Appl. Phys. Lett. 51, 1580 (1987).
5. S. Hirata, H. Narui, and O. Kumagai, Electron. Lett. 24, 239, (1988).
6. Y. Suematsu and S. Arai, Proc. of the IEEE, 75, 1472 (1987).
7. D.R. Scifres, R.D. Burnham, and W. Streifer, Appl. Phys. Lett. 26, 48 (1975).
8. G.A. Evans, N.W. Carlson, J.M. Hammer, M. Lurie, J.K. Butler, S.L. Palfrey, L.A. Carr, F.Z. Hawrylo, E.A. James, C.J. Kaiser, J.B. Kirk, and W.F. Reichert, Appl. Phys. Lett. 51, 1478 (1987).
9. S. Noda, K. Kojima, and K. Kyuma, Electron. Lett. 24, 277 (1988).
10. K. Kojima, M. Kameya, S. Noda, K. Kyuma, Electron. Lett. 24, 283 (1988).
11. H. Kogelnik and C.V. Shank, J. Appl. Phys. 43, 2327 (1972).
12. K.Y. Liou, C.A. Burrus, U. Koren, and T.L. Koch, Appl. Phys. Lett. 51, 634 (1987).
13. K. Tada, Y. Nakano, and A. Ushirokawa, Electron. Lett. 20, 82 (1984).
14. K. Utaka, S. Akiba, K. Sakai, and Y. Matsushima, IEEE J. of Quantum Electron. QE-22, 1042 (1986).
15. T. Matsuoka, Y. Yoshikuni, and H. Nagai, IEEE J. of Quantum Electron. QE-21, 1880 (1985).

16. M.C. Wu, M.M. Boenke, M. Werner, F. Schiffmann, Y.H. Lo, and S. Wang, *J. Appl. Phys.* 63, 291 (1988).
17. K. Kojima, S. Noda, K. Mitsunaga, K. Kyuma, and K. Hamanaka, *Appl. Phys. Lett.*, 50, 1705 (1987).
18. R.G. Hunsperger, *Integrated Optics: Theory and Technology*, Springer-Verlag, (1985).
19. Y. Suzuki and H. Okamoto, *J. Electron. Mats.*, Vol. 12, p. 397 (1983).
20. K.B. Kahen and J.P. Leburton, *Appl. Phys. Lett.*, Vol. 47, p. 508 (1985).
21. K. Meehan, J.M. Brown, N. Holonyak, Jr., R.D. Burnham, T.L. Paoli, and W. Streifer, *Appl. Phys. Lett.*, Vol. 44, p. 700 (1984).
22. R.M. Kolbas, N. Holonyak, Jr., B.A. Vojak, K. Hess, M. Altarelli, R.D. Dupuis, and P.D. Dapkus, *Solid State Commun.*, 31, 1033 (1979).
23. N. Holonyak, Jr., R.M. Kolbas, W.D. Laidig, M. Altarelli, R.D. Dupuis, and P.D. Dapkus, *Appl. Phys. Lett.*, 34, 502 (1979).
24. J.J. Coleman, P.D. Dapkus, B.A. Vojak, W.D. Laidig, N. Holonyak, Jr., and K. Hess, *Appl. Phys. Lett.*, 37, 15 (1980).
25. N. Holonyak, Jr., W.D. Laidig, M.D. Camras, H. Morkoc, T.J. Drummond, and K. Hess, *Solid State Commun.*, 40, 71 (1981).
26. K.Y. Hsieh, Y.C. Lo, J.H. Lee, and R.M. Kolbas, *GaAs and Related Compounds* (1988).
27. N. Holonyak, Jr., R.M. Kolbas, W.D. Laidig, B.A. Vojak, K. Hess, R.D. Dupuis, D.P. Dapkus, *J. Appl. Phys.* 51, 1328 (1980).
28. A.K. Rai, M.H. Rashid, P.P. Pronko, A. Ezis, and D.W. Langer, *J. Electron Microscopy Technique*, 5, 45 (1987).
29. J. Ralston, G.W. Wicks, L.F. Eastman, B.C. DeCooman and C.B. Carter, *J. Appl. Phys.* 59, 120 (1986).
30. D.G. Deppe and N. Holonyak, Jr., *J. Appl. Phys.* 64, R93 (1988) and references therein.
31. W.D. Laidig, N. Holonyak, Jr., M.D. Camras, K. Hess, J.J. Coleman, P.D. Dapkus and J. Bardeen, *Appl. Phys. Lett.* 38, 776, (1981).
32. K. Meehan, K.C. Hsieh, G. Costrini, R.W. Kaliski, N. Holonyak, Jr., and J.J. Coleman, *Appl. Phys. Lett.* 48, 861 (1986).

33. E.A. Dobisz, H.G. Craighead, S.A. Schwarz, P.S.D. Lin, K. Kash, L.M. Schiuvone, A. Scherer and J.P. Harbison, SPIE, Advanced Processing of Semiconductor Devices, 797, 194 (1987).
34. S. Tong Lee, G. Braustein, P. Fellingner, K.B. Kahen and G. Rajeswaran, Appl. Phys. Lett. 53, 2531 (1988).
35. E.A. Dobisz, H. Dietrich, A.W. McCormick and J.P. Harbison, Mat. Res. Soc. Symp. Proc. 147, 285 (1989).

APPENDIX I

TRIM - 87

Ion: Ga 68 890 keV

1- AlGaAs
- 5.33 g/cm³

Target
Layers 2-
3-

Ion Number : 1001

Ion Energy : 4 eV

Cascade E : 0 eV

Backscatter: 0

Transmit. : 0

AVERAGES

Mean Range : 4039 Å

Straggling : 1404 Å

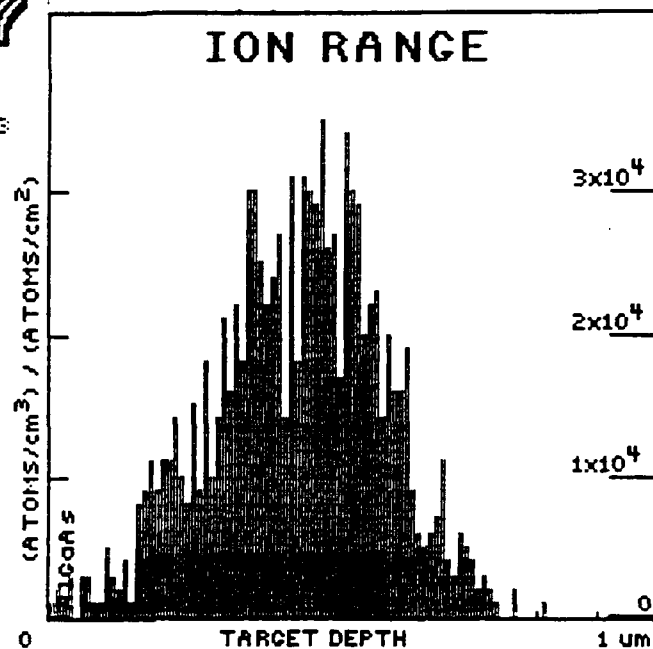
Vac./ Ion : 8404

ENERGY LOSS (%)
IONS RECOILS

Ioniz.: 32.7 21.0

Vac. : 0.5 18.3

Phon. : 0.2 27.3



(a)

TRIM - 87

Ion: Ga 68 890 keV

1- AlGaAs
- 5.33 g/cm³

Target
Layers 2-
3-

Ion Number : 1001

Ion Energy : 4 eV

Cascade E : 0 eV

Backscatter: 0

Transmit. : 0

AVERAGES

Mean Range : 4039 Å

Straggling : 1404 Å

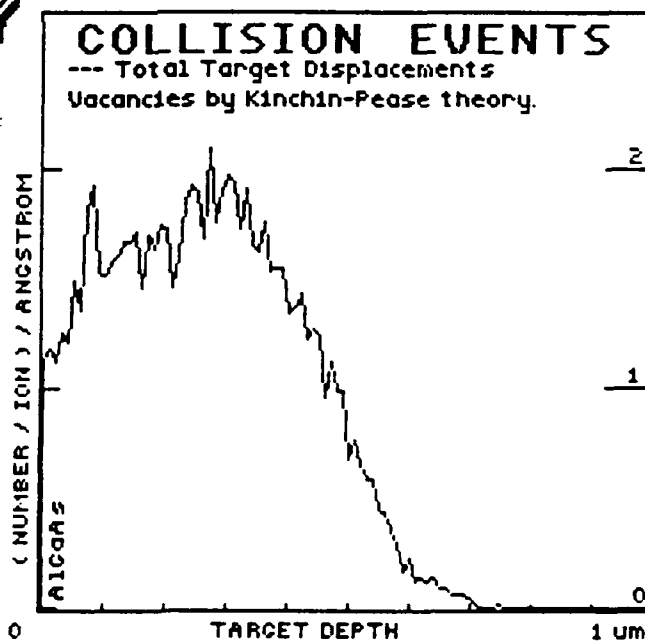
Vac./ Ion : 8404

ENERGY LOSS (%)
IONS RECOILS

Ioniz.: 32.7 21.0

Vac. : 0.5 18.3

Phon. : 0.2 27.3



(b)

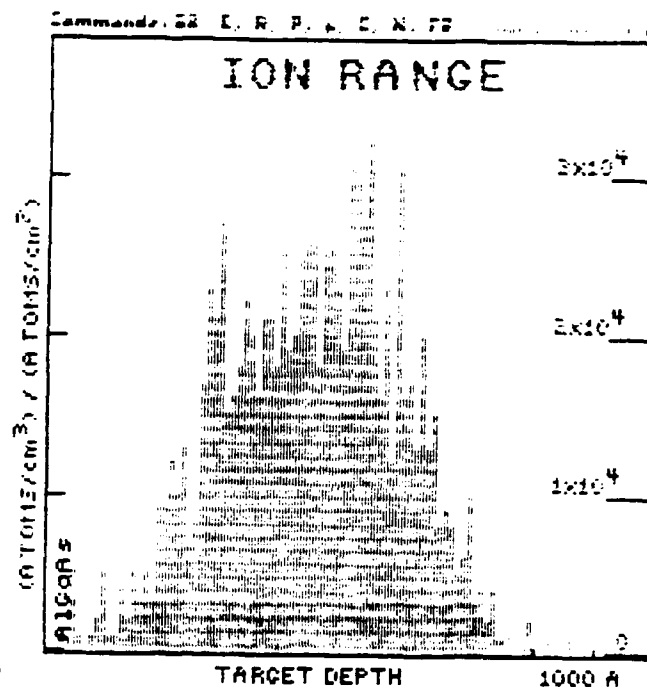
Figure 41. Ion Range and Damage Profiles for Al_{0.3}Ga_{0.7}As Implanted with 890 keV Ga.

TRIM-8.8
 68 960
 1001 - Ga keV
 2 eV
 0 eV
 0
 0

Ion Number : 1001
 Ion Energy : 2 eV
 Cascade E : 0 eV
 Backscatter: 0
 Transmitt. : 0

AVERAGE
 Mean Range : 4321 Å
 Straggling : 1472 Å
 Vac./ Ion : 8830

IONIZATION
 Ioniz: 34.4 20.6
 Vac. : 6 17.8
 Phon. : 2 26.6 0



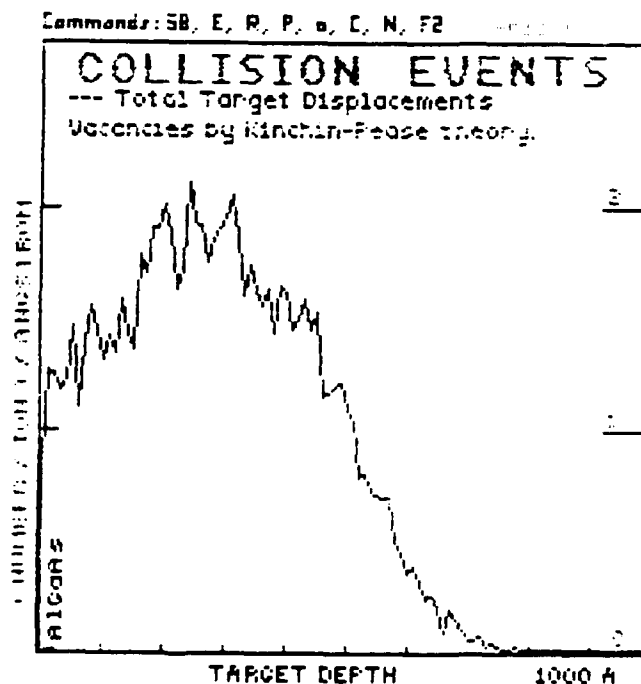
(a)

TRIM-8.8
 68 960
 1001 - Ga keV
 2 eV
 0 eV
 0
 0

Ion Number : 1001
 Ion Energy : 2 eV
 Cascade E : 0 eV
 Backscatter: 0
 Transmitt. : 0

Mean Range : 4321 Å
 Straggling : 1472 Å
 Vac./ Ion : 8830

Ioniz: 34.4 20.6
 Vac. : 6 17.8
 Phon. : 2 26.6 0



(b)

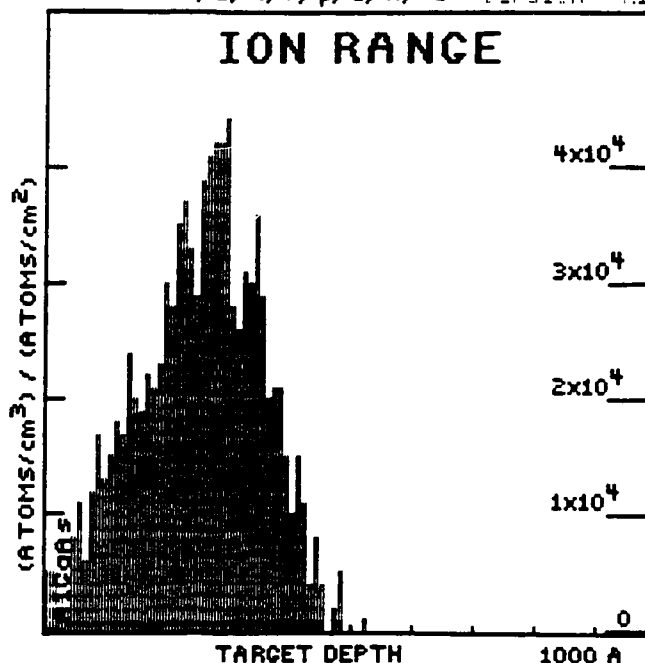
Figure 42. Ion Range and Damage Profiles for $\text{Al}_{0.3}\text{Ga}_{0.7}\text{As}$ Implanted with 960 keV Ga.

TRIM-88
 28 250
 Ion-Si keV
 1- AlGaAs
 -5.33 g/cm³
 Target
 Layers 2-
 3-

Ion Number : 1001
 Ion Energy : 4 eV
 Cascade E : 0 eV
 Backscatter: 22
 Transmitt. : 0

AVERAGES
 Mean Range : 2513 Å
 Straggling : 1004 Å
 Vac./ Ion : 2191
 ENERGY LOSS (%)
 IONS RECOILS
 Ioniz.: 44.7 13.2
 Vac. : 1.1 16.4
 Phon. : .5 24.3

Command: SB, E, R, P, p, E, N, F2 Version - 4.1



TRIM-88
 28 250
 Ion-Si keV
 1- AlGaAs
 -5.33 g/cm³
 Target
 Layers 2-
 3-

Ion Number : 1001
 Ion Energy : 4 eV
 Cascade E : 0 eV
 Backscatter: 22
 Transmitt. : 0

AVERAGES
 Mean Range : 2513 Å
 Straggling : 1004 Å
 Vac./ Ion : 2191
 ENERGY LOSS (%)
 IONS RECOILS
 Ioniz.: 44.7 13.2
 Vac. : 1.1 16.4
 Phon. : .5 24.3

Command: SB, E, R, P, p, E, N, F2 Version - 4.1

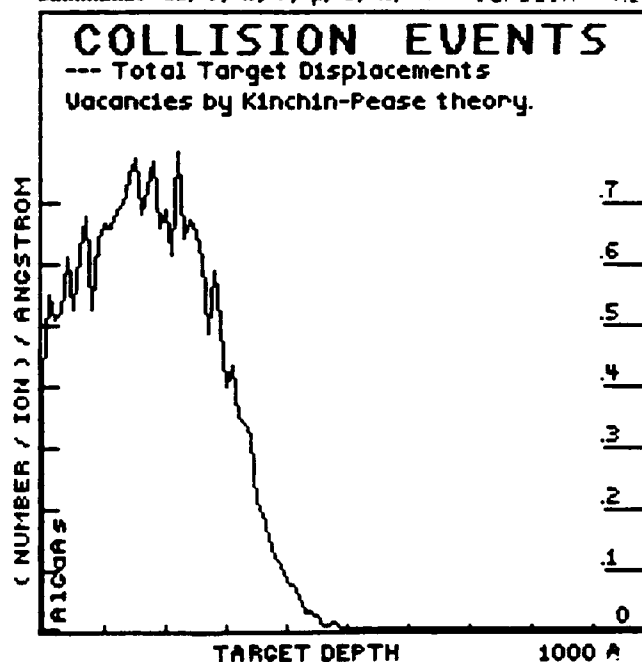


Figure 43. Ion Range and Damage Profiles for Al_{0.3}Ga_{0.7}As Implanted with 250 keV Si.